The Spitzer Extragalactic Representative Volume Survey (SERVS): Survey Definition and Goals

J.-C. Mauduit,[1] M. Lacy,[2] D. Farrah,[3] J. A. Surace,[1] M. Jarvis,[4] S. Oliver,[3] C. Maraston,[5] M. Vaccari,[6,7]
L. Marchetti,[6] G. Zeimann,[8] E. A. Gonzáles-Solares,[9] J. Pforr,[5,10] A. O. Petric,[1] B. Henriques,[2] P. A. Thomas,[2]
J. Afonso,[11,12] A. Rettura,[13] G. Wilson,[13] J. T. Falder,[4] J. E. Geach,[14] M. Huynh,[15] R. P. Norris,[16] N. Seymour,[16]
G. T. Richards,[17] S. A. Stanford,[8,18] D. M. Alexander,[19] R. H. Becker,[8,18] P. N. Best,[20] L. Bizzocchi,[11,12]
D. Bonfield,[4] N. Castro,[21] A. Cava,[21] S. Chapman,[9] N. Christopher,[22] D. L. Clements,[23] G. Covone,[24] N. Dubois,[3]
J. S. Dunlop,[20] E. Dyke,[4] A. Edge,[25] H. C. Ferguson,[26] S. Foucaud,[27] A. Franceschini,[6] R. R. Gal,[28] J. K. Grant,[29]
M. Grossi,[11,12] E. Hatziminaoglou,[30] S. Hickey,[4] J. A. Hodge,[31] J.-S. Huang,[31] R. J. Ivison,[20] M. Kim,[1] O. LeFevre,[32]
M. Lehnert,[33] C. J. Lonsdale,[1] L. M. Lubin,[8] R. J. McLure,[20] H. Messias,[11,12] A. Martínez-Sansigre,[5,22]
A. M. J. Mortier,[20] D. M. Nielsen,[34] M. Ouchi,[35] G. Parish,[4] I. Perez-Fournon,[21] M. Pierre,[36] S. Rawlings,[22]
A. Readhead,[37] S. E. Ridgway,[38] D. Rigopoulou,[22] A. K. Romer,[2] I. G. Rosebloom,[2] H. J. A. Rottgering,[39]
M. Rowan-Robinson,[23] A. Sajina,[40] C. J. Simpson,[41] I. Smail,[25] G. K. Squires,[1] J. A. Stevens,[4] R. Taylor,[29]
M. Trichas,[23] T. Urrutia,[42] E. van Kampen,[29] A. Verma,[22] and C. K. Xu[1]

[1] Infrared Processing and Analysis Center/Spitzer Science Center, California Institute of Technology, Mail Code 220-6, Pasadena, CA 91125.

[2] National Radio Astronomy Observatory, 520 Edgemont Road, Charlottesville, VA 22903.

[3] Department of Physics and Astronomy, University of Sussex, Falmer, Brighton, BN1 9QH, UK.

[4] Center for Astrophysics Research, University of Hertfordshire, Hatfield, AL10 9AB, UK.

[5] Institute of Cosmology and Gravitation, University of Portsmouth, Dennis Sciama Building, Burnaby Road, Portsmouth, PO1 3FX, UK.

[6] Department of Astronomy, Università di Padova, Vicolo dell'Osservatorio 3, 35122, Padova, Italy.

[7] Astrophysics Group, Physics Department, University of the Western Cape, Private Bag X17, 7535, Bellville, Cape Town, South Africa.

[8] Department of Physics, University of California, One Shields Avenue, Davis, CA 95616.

[9] Institute of Astronomy, University of Cambridge, Madingley Road, Cambridge, CB3 0HA, UK.

[10] National Optical Astronomy Observatory, 950 North Cherry Avenue, Tuscon, AZ 85719.

[11] Observatório Astronómico de Lisboa, Faculdade de Ciências, Universidade de Lisboa, Tapada da Ajuda, 1349-018 Lisbon, Portugal.

[12] Centro de Astronomia e Astrofísica da Universidade de Lisboa, Tapada da Ajuda, 1349-018 Lisbon, Portugal.

[13] Department of Physics and Astronomy, University of California-Riverside, 900 University Avenue, Riverside, CA 92521.

[14] Department of Physics, McGill University, Ernest Rutherford Building, 3600 rue University, Montréal, Québec H3A 2T8, Canada.

[15] International Centre for Radio Astronomy Research, University of Western Australia, M468, 35 Stirling Highway, Crawley WA 6009, Australia.

[16] Commonwealth Scientific and Industrial Research Organisation, Astronomy and Space Science, PO Box 76, Epping, NSW, 1710, Australia.

[17] Department of Physics, Drexel University, 3141 Chesnut Street, Philadelphia, PA 19014.

[18] Institute of Geophysics and Planetary Physics, Lawrence Livermore National Laboratory, 7000 East Avenue, Livermore, CA 94550.

[19] Department of Physics, University of Durham, South Road, Durham, DH1 3LE, UK.

[20] Institute for Astronomy, University of Edinburgh, Royal Observatory, Blackford Hill, Edinburgh, EH9 3HJ, UK.

[21] Institutio de Astrofísica de Canarias, C/Vía Láctea s/n, 38200, La Laguna, Tenerife, Spain.

[22] Oxford Astrophysics, Denys Wilkinson Building, Keble Road, Oxford, OX1 3RH, UK.

[23] Astrophysics Group, Blackett Laboratory, Imperial College, Prince Consort Road, London, SW7 2BW, UK.

[24] Dipartimento di Scienze Fisiche, Università Federico II and Istituto Nazionale di Fisica Nucleare, Sezione. di Napoli, Complesso Universitario di Monte S. Angelo, Via Cintia, Edificio 6, I-80126 Napoli, Italy.

[25] Institute for Computational Cosmology, Durham University, South Road, Durham, DH1 3LE, UK.

[26] Space Telescope Science Institute, 3700 San Martin Drive, Baltimore, MD 21218.

[27] Department of Earth Sciences, National Taiwan Normal University, Tingzhou Road No. 88, Section 4, Taipei 11677, Taiwan.

[28] Institute for Astronomy, University of Hawaii, 2680 Woodlawn Drive, Honolulu, HI 96822.

[29] Institute for Space Imaging Science, University of Calgary, AB T2N 1N4, Canada.

[30] European Southern Observatory, Karl-Schwartzschild-Strasse 2, 85748, Garching, Germany.

[31] Max-Planck Institute for Astronomy, Konigstuhl 17, 69177, Heidelberg, Germany.

[32] Laboratoire d'Astrophysique de Marseille, Traverse du Siphon, BP 8, 13376 Marseille Cedex 12, France.

[33] Laboratoire d'Etudes des Galaxies, Etoiles, Physique et Instrumentation GEPI, UMR8111, Observatoire de Paris, Meudon, 92195, France.

[34] Astronomy Department, University of Wisconsin, Madison, 475 North Charter Street, Madison, WI 53711.

[35] Observatories of the Carnegie Institute of Washington, 813 Santa Barbara Street, Pasadena, CA 91101.

[36] Commissariat à l'Energie Atomique, Saclay, F-91191 Gif-sur-Yvette, France.

[37] Astronomy Department, California Institute of Technology, Mail Code 247-17, 1200 East California Boulevard, Pasadena, CA 91125.

ABSTRACT. We present the Spitzer Extragalactic Representative Volume Survey (SERVS), an 18 deg^2 medium-deep survey at 3.6 and 4.5 μm with the postcryogenic *Spitzer Space Telescope* to ≈ 2 μJy (AB = 23.1) depth of five highly observed astronomical fields (ELAIS-N1, ELAIS-S1, Lockman Hole, Chandra Deep Field South, and XMM-LSS). SERVS is designed to enable the study of galaxy evolution as a function of environment from $z \sim 5$ to the present day and is the first extragalactic survey that is both large enough and deep enough to put rare objects such as luminous quasars and galaxy clusters at $z \gtrsim 1$ into their cosmological context. SERVS is designed to overlap with several key surveys at optical, near- through far-infrared, submillimeter, and radio wavelengths to provide an unprecedented view of the formation and evolution of massive galaxies. In this article, we discuss the SERVS survey design, the data processing flow from image reduction and mosaicking to catalogs, and coverage of ancillary data from other surveys in the SERVS fields. We also highlight a variety of early science results from the survey.

1. INTRODUCTION

Progress in extragalactic astronomy has been greatly enhanced by deep surveys such as the Great Observatories Origins Deep Survey (GOODS; Dickinson et al. 2003), the Cosmic Evolution Survey (COSMOS; Sanders et al. 2007), the Galaxy Mass Assembly Ultradeep Spectroscopic Survey (GMASS; Cimatti et al. 2008), and the *HST* Cosmic Assembly Near-infrared Deep Extragalactic Legacy Survey (CANDELS; Grogin et al. 2011; Koekemoer et al. 2011), which have allowed us to study the evolution of galaxies from the earliest cosmic epochs. However, a limitation of such surveys is the relatively small volumes probed, even at high redshifts: for example, Ilbert et al. (2006) find noticeable field-to-field variations in redshift distributions in the Canada-France-Hawaii Telescope Legacy Survey (CFHTLS[43]) in fields of 0.7–0.9 deg^2.

Until lately, the combination of depth and area required to map a large volume (~1 Gpc^3) of the high-redshift universe at near-infrared wavelengths, where the redshifted emission from stars in distant galaxies peaks, has been prohibitively expensive in telescope time. Two recent developments have now made this regime accessible. On the ground, the availability of wide-field near-infrared cameras has greatly improved the effectiveness of ground-based near-infrared surveys in the 1–2.5 μm wavelength range. In space, the exhaustion of the cryogenic coolant of the *Spitzer Space Telescope* opened up an opportunity to pursue large near-IR surveys using the two shortest-wavelength channels (IRAC1 [3.6] and IRAC2 [4.5]) of the Infrared Array Camera (IRAC; Fazio et al. 2004) in the postcryogenic, or "warm," mission that were much larger than was feasible during the cryogenic mission. The Spitzer Extragalactic Representative Volume Survey (SERVS), a Spitzer Exploration Science program, stems from these two developments.

SERVS is designed to open up a medium-depth, medium-area part of parameter space in the near-infrared covering 18 deg^2 to ≈ 2 μJy in the *Spitzer* [3.6] and [4.5] bands, as shown in Fig. 1 (depths were calculated using the Spitzer performance estimation tool).[44] These observations required 1400 hr of telescope time and covered five highly observed astronomical fields: ELAIS-N1 (hereafter EN1), ELAIS-S1 (ES1), Lockman Hole (Lockman), Chandra Deep Field South (CDFS), and XMM-large-scale structure (XMM-LSS). The five SERVS fields are centered on, or close to, those of corresponding fields surveyed by the shallower Spitzer Wide-area Infrared Extragalactic Survey (SWIRE; Lonsdale et al. 2003), and they overlap with several other major surveys covering wavelengths from the X-ray to the radio. Of particular importance is near-infrared data, as these allow accurate photometric redshifts to be obtained for high redshifts (van Dokkum et al. 2006; Brammer et al. 2008; Ilbert et al. 2009; Cardamone et al. 2010): SERVS overlaps exactly with the 12 deg^2 of the VISTA Deep Extragalactic Observations (VISTA VIDEO; Jarvis et al. 2012, in preparation) survey (Z, Y, J, H, and K_s bands) in the south and is covered by the UKIRT Infrared Deep Sky Survey (UKIDSS; Lawrence et al. 2007) survey (J, K) in the north. SERVS also has good overlap with the Herschel Multitiered Extragalactic Survey (HerMES; Oliver et al. 2012) in the far-infrared, which covers the SWIRE and other *Spitzer* survey fields, with deeper subfields within many of the SERVS fields.

Sampling a volume of ~0.8 Gpc^3 from redshifts 1 to 5, the survey is large enough to contain significant numbers of rare objects, such as luminous quasars, ultraluminous infrared galaxies, radio galaxies, and galaxy clusters, while still being deep enough to find L^* galaxies out to $z \approx 5$. (See, for example, Falder et al. [2011] and Capak et al. [2011], who find two galaxies in the $z = 5.3$ cluster bright enough to be detected by SERVS at 4.5 μm.) For comparison, the largest structures seen
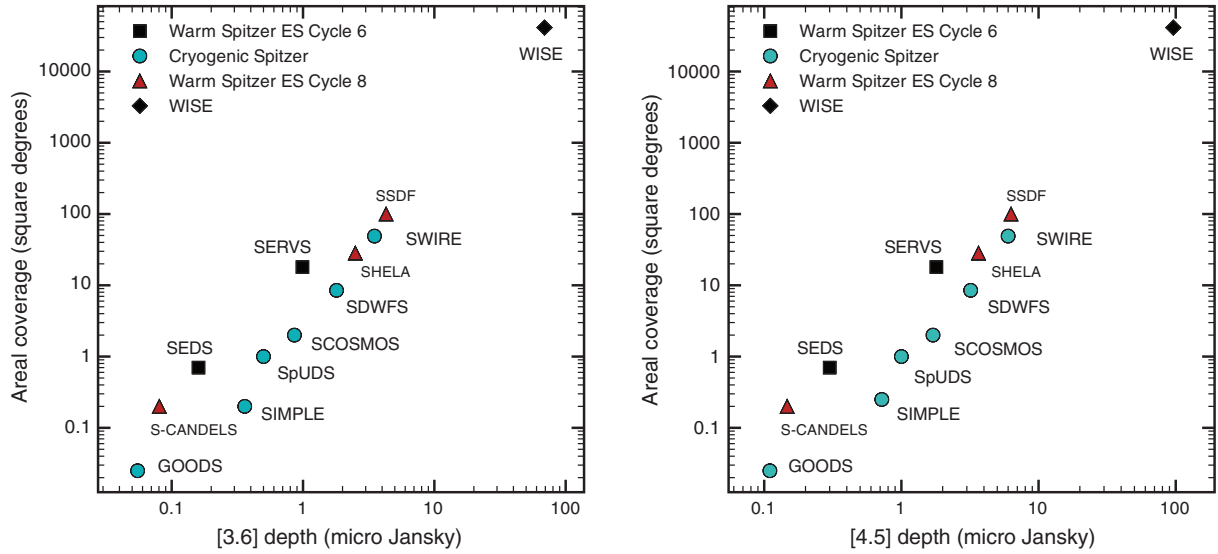
FIG. 1.—Area versus depth for SERVS compared to other surveys at wavelengths of (*left panel*) and (*right panel*). For consistency, the depth shown is the 5σ limiting flux for point sources, excluding confusion noise (as described in Section 4.2), calculated from the *Spitzer* performance estimation tool (http://ssc.spitzer.caltech.edu/ warmmission/propkit/pet/senspet /index.html) in each case. The surveys are (*from left to right*): GOODS, the *Spitzer* follow-up to the CANDELS *HST* survey (Cosmic Assembly Near-IR Deep Extragalactic Legacy Survey, Grogin et al. 2011), the *Spitzer* Extragalactic Deep Survey (SEDS, Program identifier—hereafter PID-60022, 61040, 61041, 61042, 61043, P.I. G. Fazio), the *Spitzer* IRAC/MUSYC Public Legacy in E-CDFS (SIMPLE) survey (*Spitzer*, PID 20708), the *Spitzer* Ultra Deep Survey (SpUDS, PID 40021, P.I. J.S. Dunlop), S-COSMOS, the *Spitzer* Deep Wide-Field Survey (SDWFS, Ashby et al. 2009), the *Spitzer*-HETDEX Exploratory Large Area (SHELA, PID 80100, P.I. C. Papovich) Survey, SWIRE, the SPT-*Spitzer* Deep Field (SSDF, PID 80096, P.I. S. Stanford) and the Wide-Field Infrared Explorer (WISE, Wright et al. 2010).

in the Millennium simulation at $z \sim 1$ are of the order of 100 Mpc (Springel et al. 2005), which subtends 3° at that redshift, so each SERVS field samples a wide range of environments. By combining the five different fields of SERVS, the survey effectively averages over large-scale structure and presents a representative picture of the average properties of galaxies in the high-redshift universe.

Spitzer observations of the five SERVS fields are presented in detail in § 2. Image processing is detailed in § 3, focusing on the mosaicking process and uniformity of coverage. § 4 presents the extracted SERVS catalogs, as well as an assessment of overall data quality, detection limits, and expected number counts. § 5 gives an overview of the ancillary data available at different wavelengths in the five fields. Preliminary science results and science goals are described in § 6. A summary of the SERVS data at hand is provided in § 7.

2. *Spitzer* OBSERVATIONS

2.1. Selection of Fields

SERVS consists of five fields located near the centers of corresponding SWIRE fields: EN1, ES1, Lockman, XMM-LSS, and CDFS. The SWIRE fields are in regions with low-infrared backgrounds (Lonsdale et al. 2003), making them ideal for follow-up at far-infrared wavelengths. The SERVS fields were selected to have good overlap with current and proposed surveys

in other wavebands within the SWIRE fields (see § 1), to cover both northern and southern hemispheres and to have a range in right ascension allowing both flexible follow-up with ground-based telescopes and good scheduling opportunities for *Spitzer*. Field geometry and observation details are given in Tables 1 and 2. The observed SERVS mosaics are shown in Figures 2–6, together with the coverage of significant overlapping surveys (see § 5 for an exhaustive list of all ancillary data in and near the SERVS fields).

A small fraction of the SERVS area was already covered by other deep surveys with IRAC, such as the Spitzer IRAC/ MUSYC Public Legacy in E-CDFS survey (SIMPLE, PID 20708; PI P. van Dokkum; Damen et al. 2009) in the CDFS field and the Spitzer Ultra Deep Survey (SpUDS, PID 40021; PI J.S. Dunlop) in XMM-LSS. In order to minimize the total required telescope time, these particular areas were not observed. A selection of the IRAC [3.6] and [4.5] data from these surveys (both of which also use the 100 s frame time) are therefore subsequently added into the final SERVS mosaics to attain an approximately uniform overall depth (see details in § 3.3).

In addition to this preexisting *Spitzer* data, there are also two smaller deep fields located in the SERVS area: AORID[45] 4402688 in Lockman (PID 64; PI Fazio) and the overlapping

―――――――

[45] An individual *Spitzer* observation sequence is an Astronomical Observation Request (AOR).

TABLE 1
GEOMETRY OF SERVS FIELDS

Field name	Field center R.A., decl. (J2000)	Field P.A. (deg)	Field area (deg^2)	Vertices[a] of the area covered by both [3.6] and [4.5] (deg)			
EN1	16:10:00, +54:30	350	2.0	(244.2,54.2)	(243.1,55.4)	(240.9,54.8)	(241.7,53.6)
ES1	00:37:48, −44:00	0	3	(10.5, −44.9)	(10.4,−42.9)	(8.4,−43.0)	(8.4,−45.1)
Lockman	10:49:12, +58:07	328	4.0	(165.0,57.4)	(161.7,59.8)	(159.3,59.0)	(162.7,56.4)
CDFS	03:32:19, −28:06	0	4.5	(54.4,−27.1)	(51.8,−27.0)	(51.7,−28.9)	(54.4,−28.9)
XMM-LSS	02:20:00, −04:48	0	4.5	(37.2,−5.4)	(37.0,−3.9)	(33.9,−4.1)	(34.3,−5.7)

[a] Single-band catalogs extend beyond vertices.

pointings of AORIDs 6005016 (PID 196, PI Dickinson) and 10092288 (PID 3407, PI Yan) in EN1. We deliberately reimaged them as part of SERVS so that the data taken during the postcryogenic period could be compared with the data taken earlier in the mission, and their small size made tiling around them very inefficient.

2.2. Design of Observations

The design of the SERVS observations reflected several tradeoffs to ensure efficient use of the telescope, accurate filling of the fixed field geometries, and reasonably flexible scheduling. The SERVS depth was selected so that the confusion level just became significant; attempts to make it much deeper would require better ancillary data (e.g., GOODS) reaching in the confusion noise (the rate at which depth is achieved no longer decreases as the square root of exposure time). Within the constraints of the call for proposals, at this depth, SERVS is the largest area that can easily be surveyed and that has matching ancillary data. The depth of SERVS allows us to detect all massive ($>10^{11}$ $M_\odot$) galaxies out to $z \sim 4$ (see § 4.3): essentially, the entire range of redshift over which they are seen. SERVS can thus trace the evolution of these objects from their formation until the present epoch. As a consequence of those factors, the survey covers 18 deg^2 and reaches down to ≈ 2 μJy in the *Spitzer* [3.6] and [4.5] bands.

Each field was observed in two distinct epochs, with the difference in time between the two epochs ranging from a few days to several months.[46] This allows us to reject asteroids and also gives a better photometric accuracy by ensuring that most objects appear in very different places on the array in the two sets of observations. It arises from both a half-array offset in array coordinated between the two epochs and the fact that the time difference between the execution of each epoch results in a difference in the field rotation and, hence, a different map grid for the two different epochs. Figure 7 shows the coverage of the two different epochs of observation in the EN1 field.

Toward the end of the IRAC warm-instrument characterization, several tests were performed on variations of the SERVS AORs to establish which observation strategy was optimal. Three strategies were tested, all using the small cycling dither pattern, which allows for good coverage while ensuring that objects are shifted by a minimum of several arcseconds between observations. The three strategies considered were (1) two epochs of three dithered 200 s frames, (2) two epochs of three dithered pairs of repeated 100 s frames, and (3) two epochs of six 100 s frames. In theory, strategy 1 is the most efficient and should result in a lower read-noise contribution. However, in practice, artifacts from bright stars were strong, reducing the effective area, and the radiation hit (hereafter rad hit) numbers were high (each array receives approximately 1.5 hits per second, each affecting on average two pixels, as detailed in the IRAC instrument handbook),[47] resulting in a few rad hits leaking through into the final mosaic. There was also no measurable improvement in noise level compared with the other two options, which used 100 s frames. Option 2 was almost as efficient as option 1, as only a fraction of a second was added to the overheads (the 200 s frames have a longer readout time than the 100 s frames), but image persistence effects were significant. Option 3 was therefore adopted, resulting in a very robust survey at the expense of only $\approx 3\%$ of extra observing time.

The performance of the IRAC camera (both optically, in terms of PSF and array distortion, and in terms of sensitivity) was similar to cryogenic performance; hence, the survey design was not modified because of array temperature changes. The sensitivity of the [3.6] band was affected at the 7% level by a change in the array bias between the taking of the early and later SERVS fields (see details of the calibration issues in § 3.2), but this variation was not seen as significant enough to warrant a change in survey strategy.

The mapping strategy used the small cycling dither pattern, which ensured full coverage with our map spacing of 280″. However, each epoch of a SERVS field takes long enough to

---

[46] When the scheduling gap was in months, the AORs were redesigned at the time of the observations in order to maintain proper alignment of the tiles.

[47] The IRAC instrument handbook can be found at http://irsa.ipac.caltech.edu/data/SPITZER/docs/irac/iracinstrumenthandbook/.

TABLE 2
OBSERVING LOG AND IRAC INSTRUMENT SETTINGS FOR SERVS FIELDS

Field and epoch	Dates observed	IRAC campaign(s)	Spitzer ID	Array T (K)	[3.6] bias (mV)	[4.5] bias (mV)
EN1 epoch 1	2009-07-28 to 2009-08-01	PC1	61050	31	450	450
EN1 epoch 2	2009-08-02 to 2009-08-05	PC1	61050	31	450	450
ES1 epoch 1	2009-08-06 to 2009-08-11	PC1	61051	31	450	450
ES1 epoch 2	2009-08-14 to 2009-08-18	PC2	61051	≈29[a]	450	450
Lockman epoch 1	2009-12-10 to 2009-12-21	PC10, PC11	61053	28.7	500	500
Lockman epoch 2	2009-12-25 to 2010-01-04	PC11, PC12	61053	28.7	500	500
CDFS epoch 1	2010-11-01 to 2010-11-13	PC33, PC34	61052	28.7	500	500
CDFS epoch 2[b]	2009-10-13 to 2009-10-28	PC6, PC7	61052	28.7	500	500
XMM-LSS epoch 1	2010-10-01 to 2010-10-18	PC31, PC32	60024	28.7	500	500
XMM-LSS epoch 2	2011-02-19 to 2011-03-06	PC42	60024	28.7	500	500

[a] The array temperatures were allowed to float in campaign PC2.

[b] Epoch 2 of CDFS was observed before epoch 1, which proved to be unschedulable in its originally planned slot.

observe that the field rotation changes significantly between the start and end of a single epoch of observations. Therefore, it needed to be robust against the 7° field rotation between AORs expected in an ≈10 day window in most SERVS fields. To allow for this, and to allow for accurate filling out of fixed field geometries, the SERVS AORs were kept relatively small (3× 3 maps of $5' \times 5'$ frames) and spaced closely enough to ensure

overlap for the largest expected field rotation. The small AORs also had the advantage of being easier to schedule, allowing the placement of downlinks and the insertion of short non-SERVS observations.
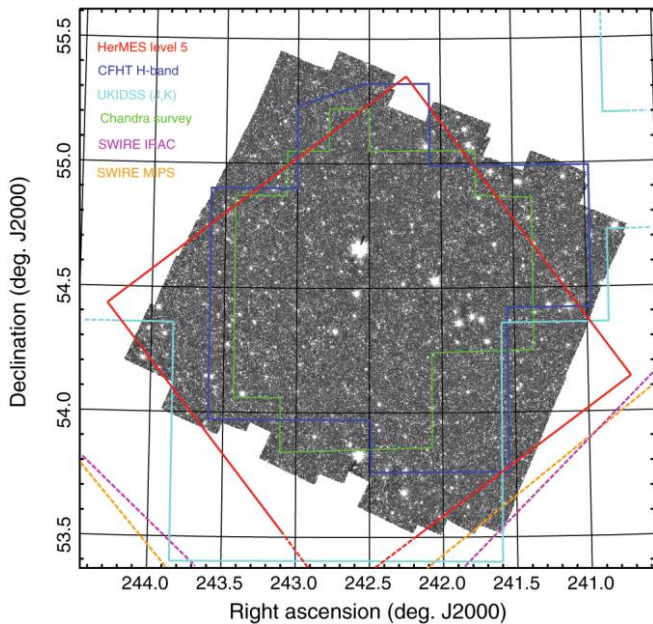

FIG. 2.—The [3.6] SERVS mosaic image of the EN1 field. Surveys of comparable size are shown here, such as HerMES level 5 (*in red*, see Oliver et al. 2012 for details), CFHT H-band (*dark blue*), UKIDSS & -bands (*light blue*), the Chandra X-ray survey (*green*), SWIRE IRAC (*dashed magenta*) and SWIRE MIPS (*dashed orange*). Surveys encompassing the entire SERVS field such as HerMES Level 6 and the GMRT survey at 610 MHz are not shown here. More details about ancillary data coverage can be found in Section 5.
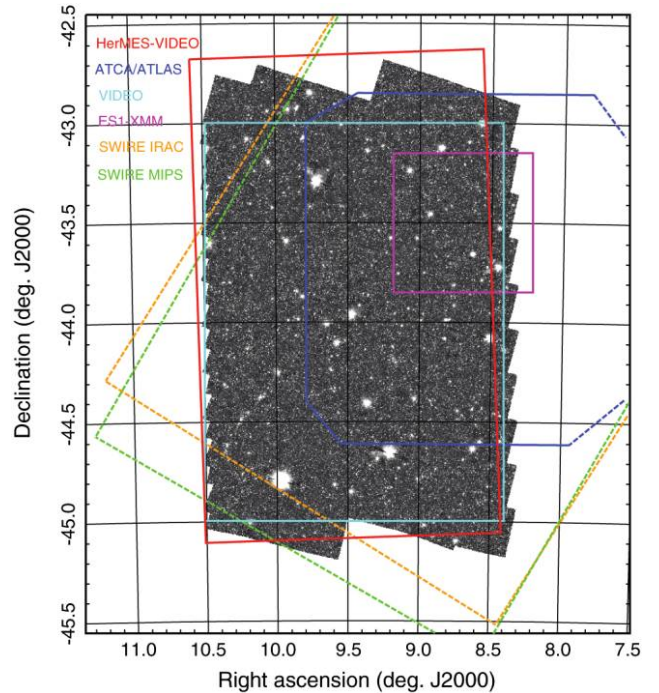

FIG. 3.—The [3.6] SERVS mosaic image of the ES1 field. Surveys of comparable size are shown here, such as the HerMES—VIDEO field (*in red*), the ATCA/ATLAS radio survey (*dark blue*), the VIDEO survey (*light blue*), the deep ES1-XMM field of Feruglio et al. (2008) (*magenta*), SWIRE IRAC (*dashed orange*) and SWIRE MIPS (*dashed green*). Surveys encompassing the entire field such as HerMES Level 6 are not shown here. More details about ancillary data coverage can be found in Section 5.
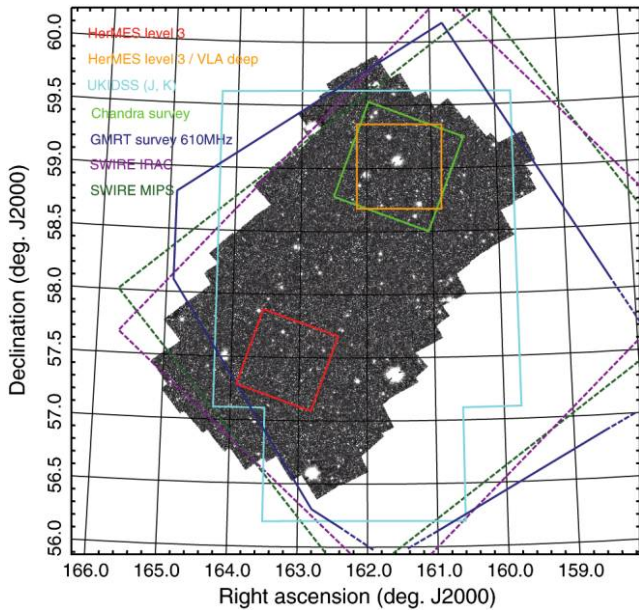
The total observing times for EN1, ES1, Lockman, CDFS, and XMM-LSS were 153.4 hr, 231.8 hr, 354.5 hr, 319.1 hr, and 323.2 hr, respectively. The mean integration time per pixel of the resulting SERVS mosaics is close to the design depth at ≈ 1200 s. There are, however, both regions of significantly deeper data where AORs and map dithers overlap and shallower areas, particularly around the edges, where one epoch is affected by scattered light from a field star. Uniformity of coverage of the five SERVS fields is discussed in detail in § 3.3.

3. DATA PROCESSING

SERVS data are available from the Spitzer Heritage Archive.[48] SERVS mosaics (image, coverage, uncertainty, and mask mosaics), and catalogs, including ancillary data at other wavelengths taken as part of SERVS will be made available to the community during the summer of 2012, ultimately through the Infrared Science Archive (IRSA). Catalogs containing the full data set of ancillary data will be described in detail in Vaccari et al. 2012, in preparation.

—————————
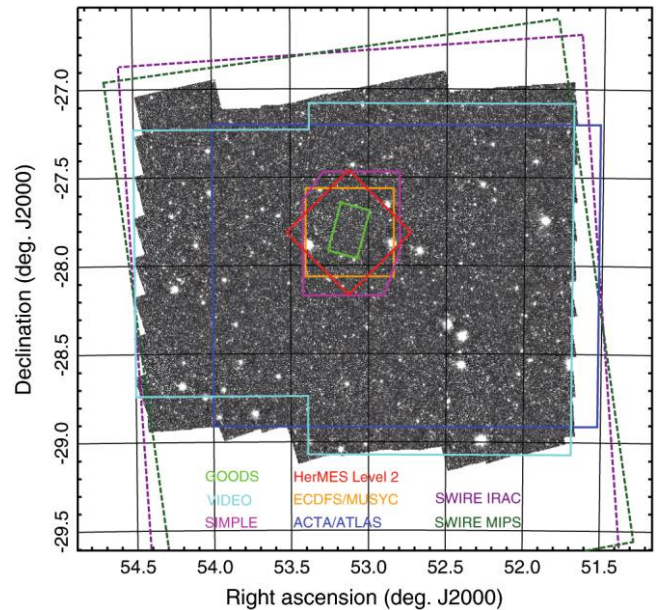
[48] See http://sha.ipac.caltech.edu/applications/Spitzer/SHA/.

3.1. Image Postprocessing and Mosaics

Data processing begins with the basic calibrated data image, produced by the Spitzer Science Center (SSC).[49] These images have been dark-subtracted and flat-fielded and have had astrometric and photometric calibration applied. A pipeline[50] originally used for processing SWIRE data was improved and applied to the SERVS data to further clean the frames of artifacts. Specifically, this pipeline fixed an artifact called "*column pull-down*"[51] found near bright stars and also corrected interframe bias offsets by setting the background equal to that of a COBE-based model of the zodiacal background (the dominant background at these wavelengths). Due to the inability to use the IRAC shutter, all IRAC data suffer from a variable instrument bias level known as the "first-frame effect,"[52] which varies depending on the recent detector history. Thus, no measurement of the true infrared background, or of any spatial structure within the background larger than the array size of 5′, is possible.

—————————

[49] See http://ssc.spitzer.caltech.edu/.

[50] See http://irsa.ipac.caltech.edu/data/SPITZER/SWIRE/.

[51] The *column pull-down* effect, which manifests in the slow-read direction (columns) of the detectors at 3.6 and 4.5 μm, is a depression in the zero level of the column.

[52] The IRAC instrument handbook can be found at http://irsa.ipac.caltech.edu/data/SPITZER/docs/irac/iracinstrumenthandbook/.
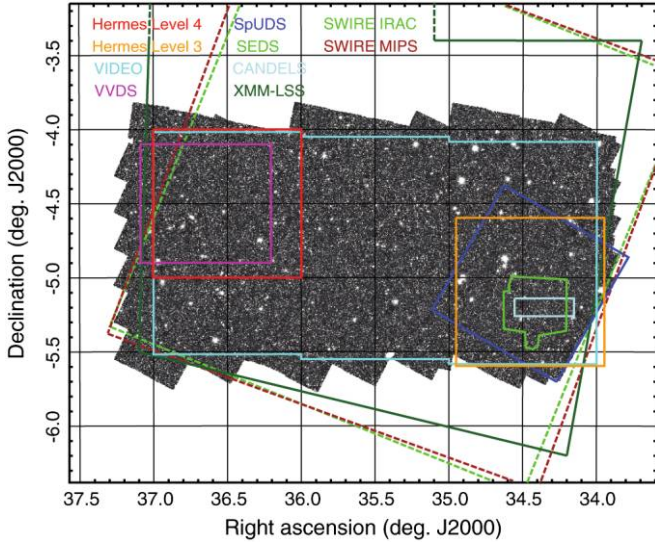
FIG. 6.—The [3.6] SERVS mosaic image of the XMM-LSS field. The two HerMES Level 4 & 3 pointings are shown in *red* and *orange*. The VIDEO pointing is featured in *cyan* and VVDS in *magenta*. The Eastern fields correspond to the SpuDS (*blue*), SEDS (*green*) and CANDELS (*light grey*). XMM-LSS is shown in (*dark green*) and extends beyond the SERVS CDFS field limits. SWIRE IRAC is shown as *dashed green* and SWIRE MIPS as *dashed brown*. Surveys encompassing the entire field such as HerMES Level 6 are not shown here. More details about ancillary data coverage can be found in Section 5.
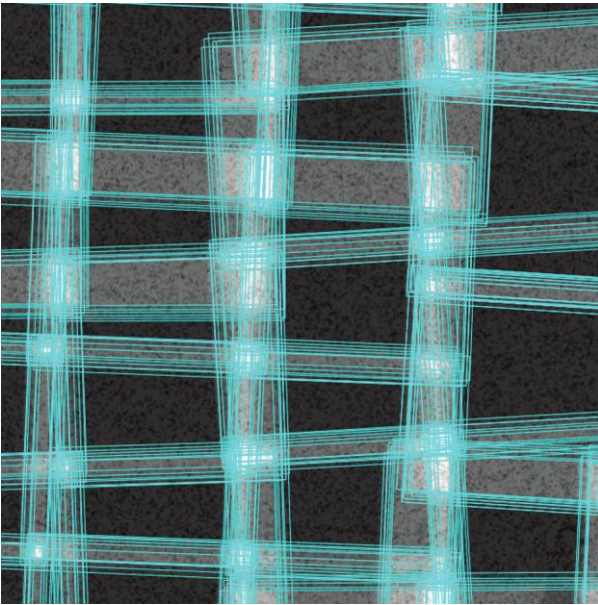

FIG. 7.—A detail of the data coverage in the EN1 field at 3.6 μm. The image is 12″ across. The *cyan* lines indicate the array edges of the individual input images and the *greyscale* underneath shows the mosaic coverage depth, ranging from 12 to 35 frames. The non-uniform depth of coverage seen above is reflected in the cumulative distribution function of Fig 12.
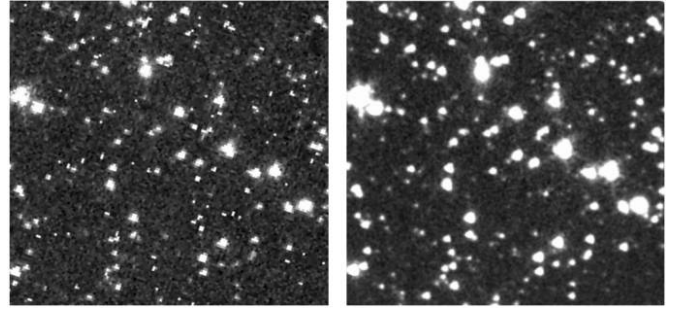

FIG. 8.—*Left*: An example of a SERVS reduced single 100 s exposure frame at [3.6]. The frame size is . *Right*: the final coadded [3.6] image.

The data were co-added (see Fig. 8) using the MOPEX[53] package available from the SSC (parameters used are listed in Table 3). All the data from a single field were co-added onto a single frame; the two different wavelengths are reprojected to the same astrometric projection so that their pixels align one to one. The data are reprojected with a linear interpolation onto a pixel scale of 0.6″, providing marginal sampling at 3.6 μm. The multiple dithers allow at least some recovery from the severe undersampling of the IRAC camera at these wavelengths.

The depth reached by the SERVS observations can easily be put in perspective when comparing SWIRE and SERVS cutouts of a similar region of sky (*left* and *right*, respectively, in Fig. 9). With a depth of 3.7 μJy at [3.6] and 7.4 μJy at [4.5], SWIRE is limited to $z \approx 1.5$ for L^* galaxies, whereas SERVS can detect these galaxies up to $z \sim 4$ (see § 4.3).

Large mosaics containing all the SERVS epochs of observation in each field were created from the co-added images, along with the uncertainty, coverage, and mask images (see Fig. 10). The resulting mosaics cover areas of ~2, 3, 4, 4.5, and 4.5 deg^2 for EN1, ES1, Lockman, CDFS, and XMM-LSS, respectively (see Table 1 for details about the geometry of the five fields).

3.2. Calibration Issues

The initial observations (all of EN1 and the first half of ES1) were made before the IRAC detectors were stabilized at their current operating temperature of 28.7 K, which is now the norm for the *Spitzer* postcryogenic (i.e., "warm") mission (see Table 2). Instead, these data were taken at a controlled temperature of 31 K. The second half of ES1 was taken during a time when the detector was cooling from 31 K to the final temperature of 28.7 K and was not under active temperature control. In addition, during this time period, the detector biases for both arrays were adjusted. These changes in temperature and detector operating parameters resulted in changes to both the instrument calibration and its noise properties. These were only measurable

---

[53]MOPEX and its associated documentation can be obtained at http://irsa.ipac.caltech.edu/data/SPITZER/docs/dataanalysistools/tools/MOPEX/.

TABLE 3
VALUES OF MORE IMPORTANT MOPEX AND SEXTRACTOR PARAMETERS

Program (module)	Parameter	Value
MOPEX (DETECT)	Detection_Max_Area	100
MOPEX (DETECT)	Detection_Min_Area	0
MOPEX (DETECT)	Detection_Threshold	4
MOPEX (MOSAICINT)	INTERP_METHOD	1
MOPEX (MOSAICDUALOUTLIER)	MIN_OUTL_IMAGE	2
MOPEX (MOSAICDUALOUTLIER)	MIN_OUTL_FRAC	0.51
MOPEX (MOSAICOUTLIER)	THRESH_OPTION	1
MOPEX (MOSAICOUTLIER)	BOTTOM_THRESHOLD	0
MOPEX (MOSAICOUTLIER)	TOP_THRESHOLD	0
MOPEX (MOSAICOUTLIER)	MIN_PIX_NUM	3
MOPEX (MOSAICRMASK)	MIN_COVERAGE	4
MOPEX (MOSAICRMASK)	MAX_COVERAGE	100
SExtractor	DETECT_MINAREA	5.0
SExtractor	DETECT_THRESH	0.4
SExtractor	ANALYSIS_THRESH	0.4
SExtractor	FILTER	Default
SExtractor	DEBLEND_NTHRESH	64
SExtractor	DEBLEND_MINCONT	0.005
SExtractor	SEEING_FWHM	2.0
SExtractor	BACK_SIZE	32
SExtractor	BACK_FILTERSIZE	5
SExtractor	BACKPHOTO_TYPE	LOCAL
SExtractor	WEIGHT_TYPE	MAP_WEIGHT[a]

NOTE.—Similar values can be found in Lacy et al. (2005) and Ashby et al. (2009).

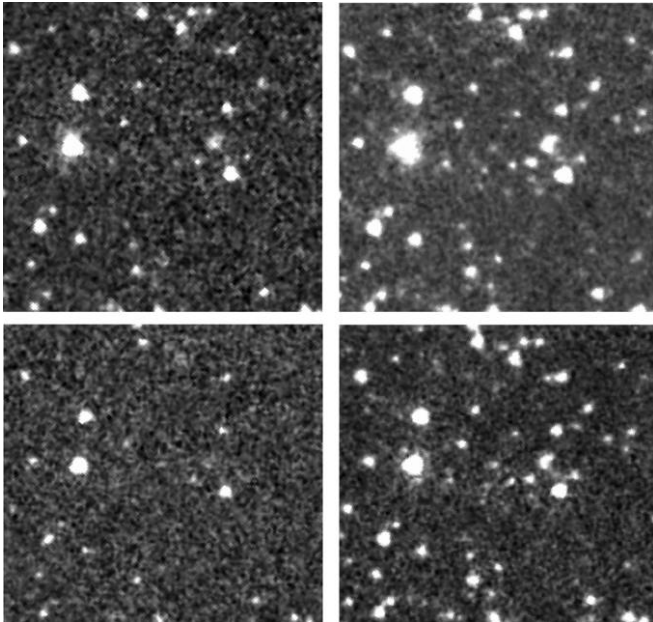[a] Using coverage map as inverse variance weight map.

FIG. 9.—A cutout of the EN1 field at [3.6] (*top panel*) & [4.5] (*bottom panel*), as imaged by SWIRE (*left*) & SERVS (*right*). The difference in depth between the two surveys can clearly be seen here.

in the [3.6] band, resulting in an $\approx 7\%$ increase in the noise in EN1 and ES1 at [3.6] compared with the remainder of the survey.

IRAC is calibrated based on dedicated calibration observations collected during science operations. These data are typically collected on timescales of years. The *Spitzer* cryogenic mission, as well as the nominal warm mission, are extremely well calibrated. However, during this transition period only a small amount of calibration data could be taken, as conditions were constantly changing. The Spitzer Science Center provided an initial calibration, which was reliable to a few percent. Photometry from SERVS was compared with that of SWIRE on an object-by-object basis, and small multiplicative offsets at the few-percent level were found. These calibration errors were fixed at the catalog level (see § 4) by applying multiplicative factors derived from comparison between sources detected both in SWIRE and SERVS. Calibration is therefore the same as that of the SWIRE data.

3.3. Uniformity of Coverage

Certain areas of the original SERVS footprint were already covered by several previous *Spitzer* surveys, such as SpUDS for XMM-LSS and SIMPLE/GOODS for CDFS (see § 2.1 for details). These regions were deliberately avoided during the SERVS observation campaign to save observation time. Since the optical properties of the camera did not change between the
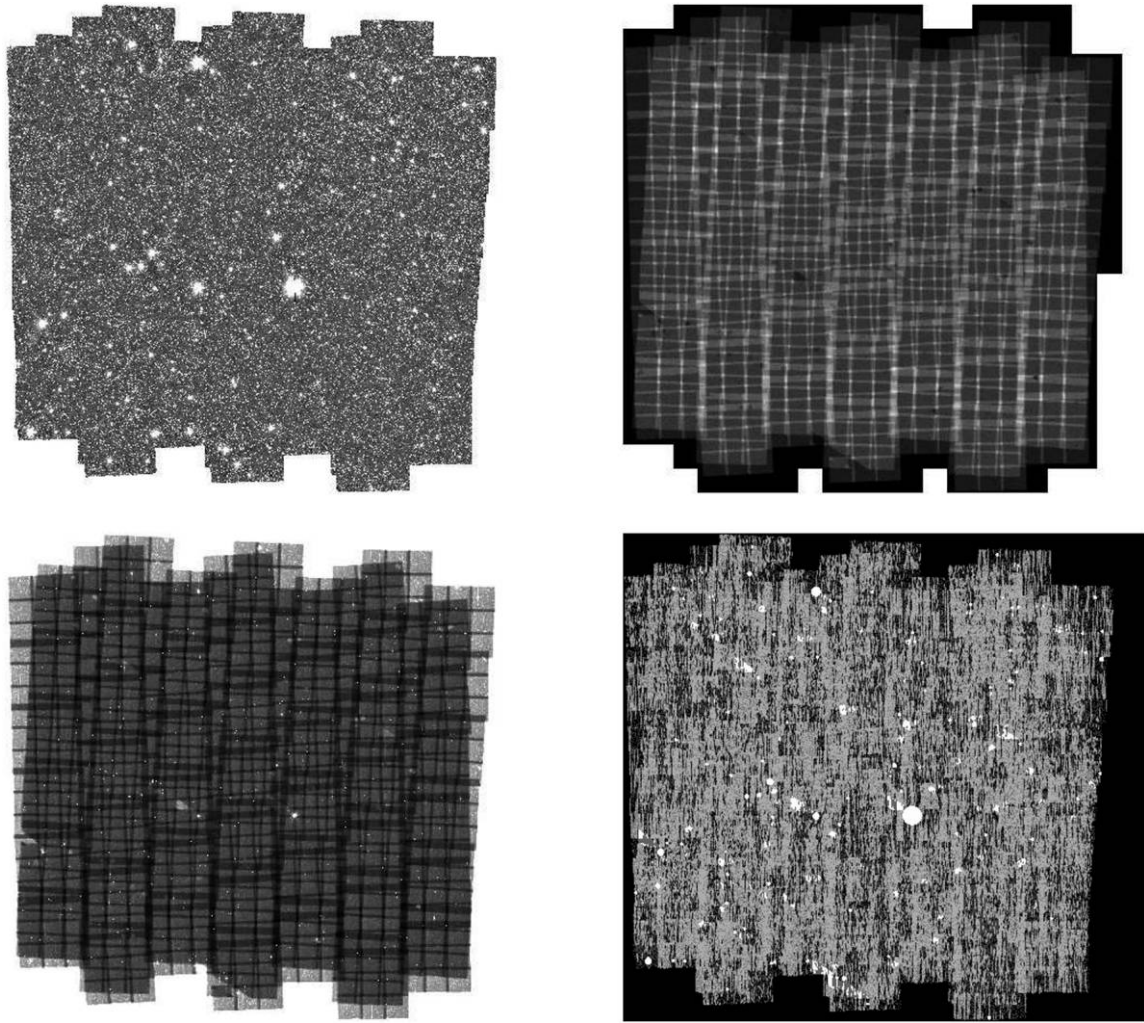
FIG. 10.—SERVS final set of mosaics for the EN1 field at 3.6 μm (*top left*: image mosaic, *top right*: coverage mosaic, *bottom left*: uncertainty mosaic, *bottom right*: mask mosaic).

cryogenic and warm missions and since all the *Spitzer* data were combined using the same MOPEX pipeline, previous survey frames were subsequently merged with the SERVS data at co-addition and patched onto the final mosaics. Given the higher depth of the previously existing smaller *Spitzer* surveys, it was always possible to reasonably match the depths of the SERVS observations in these areas by selecting the right number of single frames to co-add. In addition, since the archival data are only a minimal fraction of the survey (~12% of XMM-LSS and ~3% of CDFS, none in the other fields), these minor differences in coverage between archival and SERVS data are not an issue.

The selection of archival data was focused on filling the missing areas as best as possible and was thus not refined to be necessarily chosen from different dates of observations; hence, some contamination by transient sources on timescales

of hours is possible. Some artifacts such as *muxbleed*[54] were present in the cryogenic data and not in SERVS; however, after processing, all artifacts were removed and did not impact the mosaicking. A grid extending over the missing data was set to match the SERVS frame centers (spacing and orientation) as closely as possible. The closest SpUDS (or SIMPLE/ GOODS) frames to these grid centers were then automatically selected and a subsample of those was chosen to best cover the area and match the SERVS depth (the top panel of Fig. 11 shows the XMM-LSS field frame selection process as an example). The resulting coverage map for the XMM-LSS field is shown in the bottom panel of Figure 11 as an example.

---

[54] The muxbleed effect appears as a series of bright pixels along the fast-read direction (horizontal in array coordinates) and may extend the entire width of the array (5′).
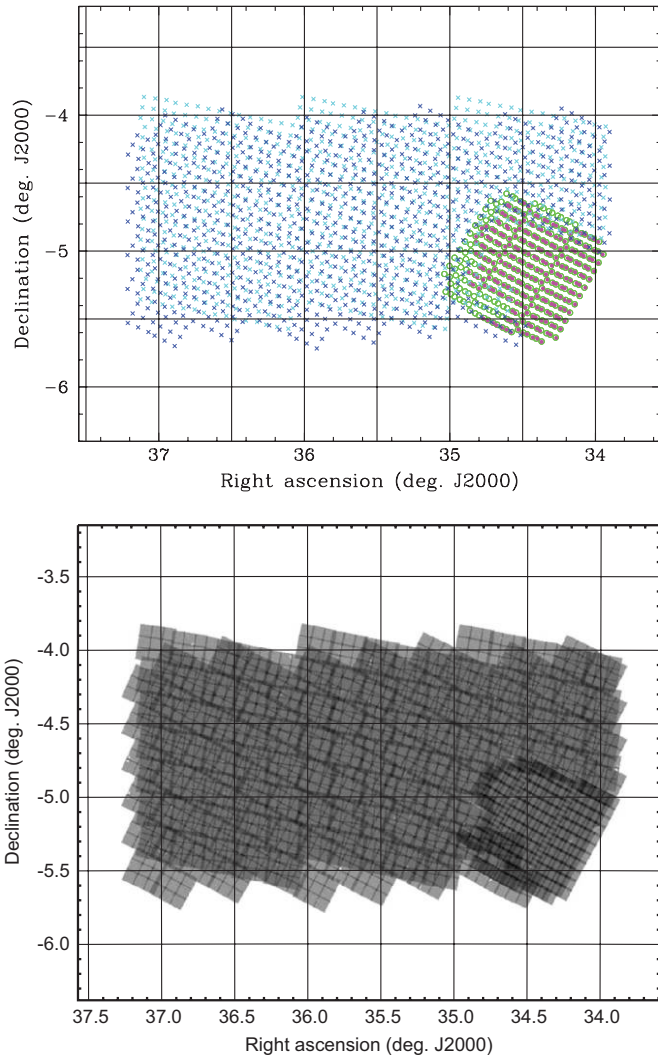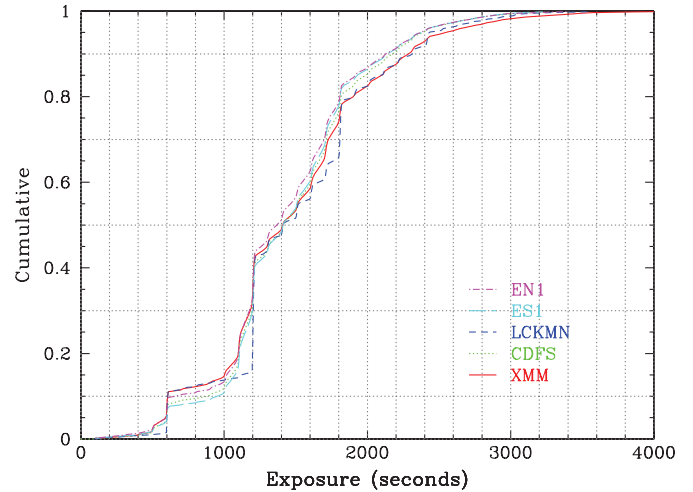
FIG. 12.—Cumulative distribution function of the coverage maps for all five fields, in terms of exposure time (in seconds). The curve represents the fraction of pixels with that integration time or lesser.

FIG. 11.—*Top*: XMM-LSS single frame centers, showing epoch 1 in *cyan* and epoch 2 in *blue* crosses (see Table 2). A grid extrapolating the XMM-LSS epoch2 geometry was overlaid onto the SpUDS field frames (*in green open circles*) and used to select the relevant SpUDS frames to co-add (*magenta solid points*) to complete the XMM-LSS field. *Bottom*: Coverage map in equatorial coordinates of the XMM-LSS field at [3.6]. Note the addition of the SpUDS data between & to patch the XMM-LSS field. The rotation in tiling induced by the choice of two different epochs of observation (of six 100 s frames each, as discussed in Section 2.2) is also clearly visible here. Coverage is not completely uniform throughout the field and data can be deeper, especially at the overlap of the SERVS (warm mission) & SpUDS (cryogenic) surveys (see Section 3.3 for details).

Coverage is thus not completely uniform throughout the fields, though averaging ~1400 s of exposure time over all five fields (see Fig. 12). By design, some overlap between AORs was allowed and some areas in a field may have a higher coverage (e.g., at the AOR intersections): for example, totaling up to ~4700 s in Lockman. Although great care was taken to minimize variations in the coverage throughout a field, the exposure time can rise up to ~5000 s (e.g., in XMM-LSS) when the added ancillary data intersect both SERVS epochs (mostly

around the edges of the SERVS/ancillary data, as is obvious in the bottom of Fig. 11). However, these areas of higher coverage represent a very small portion of the fields and do not have an impact on the overall uniformity, given the already intrinsic nonuniform nature of the SERVS coverage due to the original tiling design. The higher depths of the observations at the frames overlaps or due to archival data overlapping the SERVS frames do not result in any impact to the survey reliability or completeness when a minimum flux selection based on the SERVS data is used.

3.4. Image Masks

Bright source artifacts (stray light, column pull-down, and latents) are a significant problem with *Spitzer* data. Most of these artifacts are discussed in more detail in the IRAC instrument handbook, available from the SSC, as well as in Surace et al. (2005).[55] In order to flag for these artifacts, mask images are created for each of the five fields. Flag bit values attributed to each significant artifacts are listed in Table 4, as well as in the headers of the mask FITS files.

In addition to these known *Spitzer* image artifacts, saturated stars are common across the deep and wide SERVS fields and thus need to be flagged appropriately. Indeed, very bright stars do not have reliably extracted fluxes in SERVS and may occasionally be split into multiple fainter sources or are saturated, so no flux can be measured accurately; erroneous detections in the wings of the PSF can also cause artifacts. As a result, a safe radius has to be set and flagged around those bright stars. Luckily, any object triggering bright star artifacts in the SERVS data is easily detected by the Two Micron All Sky Survey (2MASS;

---

[55] Vizier Online Data Catalog, 2255 (J. A. Surace et al., 2004).

TABLE 4
LOOKUP TABLE FOR MASK-IMAGE BIT VALUES

Bit number	Bit value	Flag
BIT00	1	Overall data quality
BIT01	2	Set if pixel contains rad hit
BIT02	4	Set if optical ghost present
BIT03	8	Set if stray light present
BIT04	16	Set if saturation donut
BIT05	32	Set if pixel contains latent image
BIT06	64	Set if pixel is saturated
BIT07	128	Set if column pull-down present
BIT08	512	Set if bright star is present

NOTE.—Flags are described in more detail in the text in § 3.4.

TABLE 5
BRIGHT-OBJECT FLAGGING FOR MASK IMAGES

2MASS K mag. range	Radius (Arcsec)
>12.0	0
10.0–12.0	15
8.0–10.0	20
7.5–8.0	30
6.5–7.5	45
5.0–6.5	60
<5.0	120

NOTE.—The radii are taken from SWIRE (Vizier Online Data Catalog, 2255 [J. A. Surace et al., 2004]) and increased to take into account the deeper exposures of SERVS.

Skrutskie et al. 2006), which has reliable fluxes even for very bright objects. The positions and K-band magnitudes of bright stars are downloaded from the 2MASS Point Source Catalog in the Vizier database.[56] Magnitudes are thus converted into radii according to Table 5. The radii are taken from SWIRE (Surace et al. 2005) and increased to take into account the deeper exposures of SERVS. To reduce memory requirements on such large images, subsets of the mosaics were cut around each bright star, flagged, and then reembedded onto the final mask mosaic. The resulting bright star flag masks a circular region around each bright star in the fields. A part of the Lockman-field bright star mask is shown in Figure 13.

4. CATALOGS

4.1. Catalogs Extraction and Calibration

Catalogs were made using SExtractor (Bertin & Arnouts 1996). Two sets of catalogs were produced for each field (the parameters used in the source extraction are given in Table 3). The first set is based on extractions from the [3.6] and [4.5] bands, separately. A second set is then created when the two catalogs are merged, and only detections common to both are retained. This results in a high-reliability catalog that is used to combine with other data sets.For rare objects searches, we recommend using the high-reliability catalogs. The single-band catalog may be used for band-merging with other data (e.g., UKIDSS/DXS data), or for statistical studies.

SExtractor aperture fluxes are computed within radii of 1.4″, 1.9″, 2.9″, 4.1″, and 5.8″ and corrected using the aperture correction factors derived for SWIRE DR2/3 and reported in Table 6. The IRAC instrument has a calibration tied to standard stars as measured in a fiducial 12″ radius aperture. This aperture is nonideal for faint-source extraction, so the fluxes are measured in smaller apertures and suitable aperture corrections are applied.

[56] The Vizier database is available at http://vizier.u-strasbg.fr/.

A fraction of the SERVS data was taken prior to the final temperature stabilization of IRAC and prior to the selection of the final array biases (affecting the EN1 and ES1 fields; see Table 2). During this "floating-temperature" period, the IRAC calibration drifted, with changes to both the overall gain and the detector linearization, as discussed § 3.2. As a result, the images have overall calibration errors at the level of a few percent. In addition, the other fields show small, but noticeable, calibration differences compared with the cryogenic [3.6] SWIRE data. These calibration errors were fixed at the catalog level by applying multiplicative factors derived from comparison between sources detected both in SWIRE and SERVS ($f_{[3.6]\mathrm{SWIRE}}/f_{[3.6]\mathrm{SERVS}} = 1.07$ for EN1 and ES1; 1.02 for Lockman, CDFS, and XMM-LSS; at [4.5] the correction factors are very close to
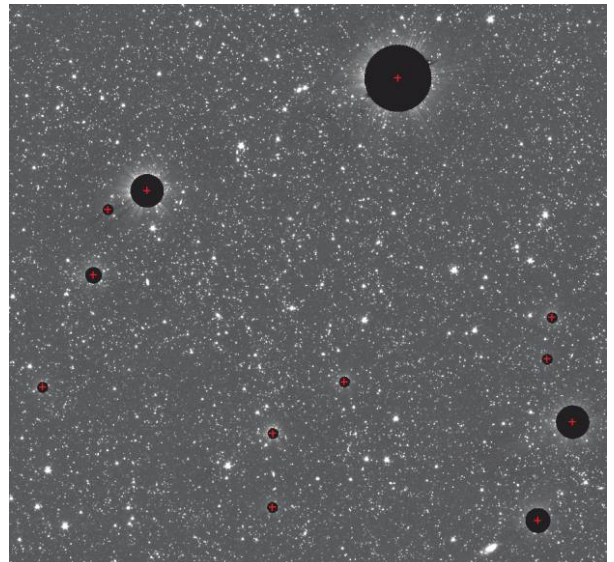

FIG. 13.—Bright star mask cutout of a portion of the Lockman field. *Black circles* show the masked regions around the cross-identified 2MASS bright stars centers (*red crosses*) in the field. Radii are proportional to 2MASS -band brightness and shown in Table 4.

TABLE 6
Aperture Sizes and Corrections

Aperture number	Aperture radii (arcsec)	[3.6] correction (arcsec)	[4.5] correction (arcsec)
ap1	1.4	0.585	0.569
ap2	1.9	0.736	0.716
ap3	2.9	0.87	0.87
ap4	4.1	0.92	0.905
ap5	5.8	0.96	0.95

Note.—Aperture sizes and corrections were derived for SWIRE (Vizier Online Data Catalog, 2255 [J. A. Surace et al., 2004]). More details can be found therein.

unity, and no corrections were applied). SERVS calibration is thus tied to that of the SWIRE data.

4.2. Number Counts and Completeness

Simple number counts were derived from the extracted catalogs. The SERVS source counts for the XMM-LSS field is provided as an example in the left part of Figure 14 (the remaining four fields are shown in Appendix A). Several features are visible in this plot. Fundamentally, the observed counts present as a power law. This is shallow at the bright end, primarily due to the presence of bright stars. There is a known break in the power-law index near 100 μJy (Glazebrook et al. 1994). At the faintest

levels, the turnover is a result of the increasing incompleteness of the survey. It is clear that the SERVS completeness level catastrophically drops near 2–3 μJy. As a consistency check, a sample of bright stars (SERVS fluxes within $0.3 < f < 2$ mJy and stellarity index >0.95) was selected. Cross-identifying with the 2MASS catalog, K-band measurements were used to compare the deviation of SERVS colors with respect to the 2MASS ones. A color-color plot of $K_{2\mathrm{MASS}} - M_{3.6\,\mu m}$ (Vega) versus $M_{3.6\,\mu m}$(Vega) $- M_{4.5\,\mu m}$ (Vega) for the XMM-LSS field, shown in the right part of Figure 14, confirms that SERVS is consistent with 2MASS.

SERVS detects $\sim 100,000$ sources per square degree and, with ~ 40 beams per source, approaches the classical definition of where source confusion becomes important. The effective depth of SERVS is thus affected by confusion noise, which makes the definition of survey depth dependent on the experiment one wishes to carry out. For a detection experiment on point-source objects detected in another waveband with a well-determined position (positional uncertainty much lower than the SERVS beam of $\approx 2''$), the appropriate number, denoted as σ_{pp}, is determined from the pixel-to-pixel variance in a source-free region of a single basic calibrated data image (assuming it scales as the square root of the coverage and that extraction is carried out by source fitting: i.e., assuming 7.0 and 7.2 noise pixels in [3.6] and [4.5], respectively). Another measure of the noise, which includes some contribution from confusion noise, is obtained from "empty-aperture" measurements,
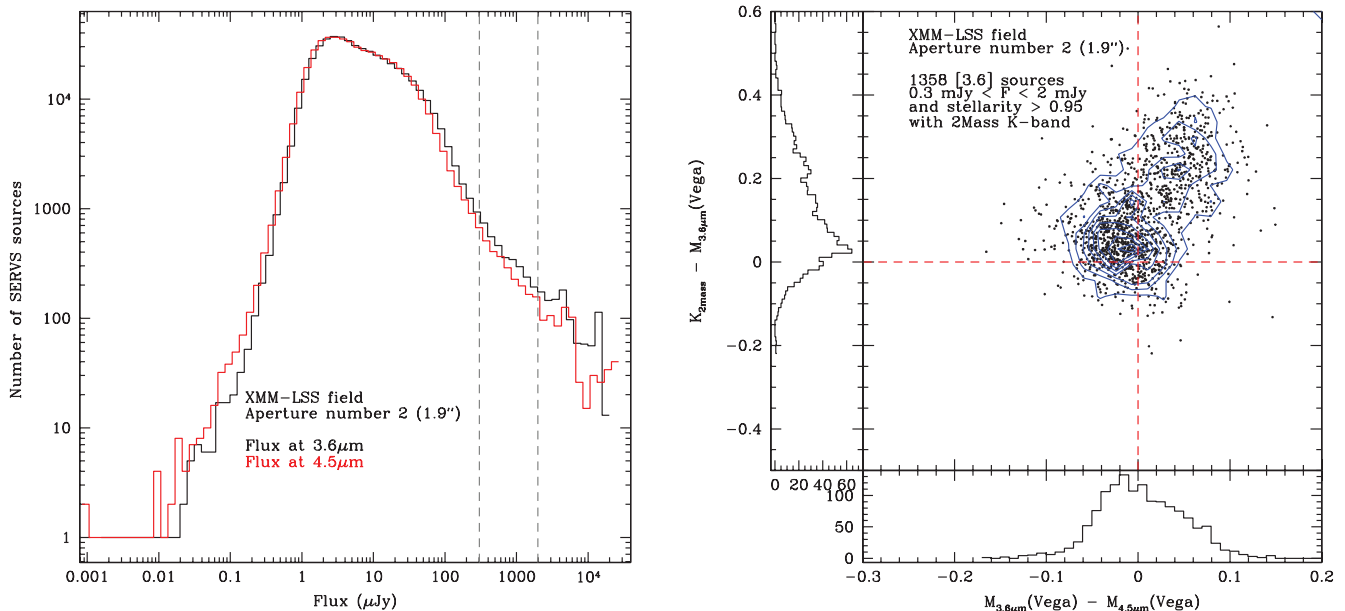

Fig. 14.—*Left*: SERVS number counts versus flux at [3.6] (*black* histogram) and [4.5] (*red* histogram) for the XMM-LSS field. Grey dashed lines show the selection of sources used in the right plot (with fluxes as). *Right*: Color-color plot showing (Vega) versus (Vega) for sources within the flux range defined by the grey dashed lines above, plus a cut in stellarity index and the existence of a 2MASS -band measurement as an additional constraint. *Red dashed* lines help pinpoint the location of the (0,0) point in this diagram. Similar plots for the EN1, ES1, Lockman & CFDS fields are shown in Appendix A.

TABLE 7
APPROXIMATE SURVEY DEPTH AND COMPLETENESS IN
SERVS FIELDS

Measurement	[3.6] value (μJy)	[4.5] value (μJy)
$5\sigma_{pp}$	1.3	1.5
$5\sigma_{ap}$	1.9	2.2
S_{50c}[a]	4.0, 3.0	3.5, 3.5
S_{80c}[a]	7, 5	5, 5

NOTE.—EN1 and ES1 are about 7% noisier than the other fields in [3.6], due to different detector settings used early in the warm mission (Table 2).

[a]The two completeness levels shown correspond to the two-band detection catalog and the single-band catalog.

where the standard deviation of fluxes in object-free apertures in the final mosaic is measured directly. For our fields, this measurement was made in 3.8″ diameter apertures (SWIRE aperture 2) and is denoted as σ_{ap}. SWIRE aperture 2 is recommended by the SWIRE team as the most stable aperture for photometry, since most faint IRAC sources are slightly resolved at the ≈ 1–$2''$ level. Survey depths for the various measurements are summarized in Table 7.

Finally, for survey work, the completeness limits at 50 and 80% (S_{c50} and S_{c80}) give a good indication of the depths that are usable for global survey properties such as source counts. Following the techniques of Chary et al. (2004) and Lacy et al. (2005), we simulated ~10,000 model galaxies, distributed them in the reduced mosaics, and extracted them using the same pipeline that created the catalogs. The recovery rate of the model galaxies was used as our completeness indicator and suggests that $\approx 50\%$ completeness is reached at a flux density of ≈ 2–$3~\mu$Jy in the single-band catalogs at both [3.6] and [4.5], due to a combination of signal-to-noise ratio and source confusion (see Fig. 15). More details of the completeness and reliability of the SERVS catalogs will be presented by Vaccari et al. (2012, in preparation).

4.3. Expected Detection Limits and Redshift Distribution

The SERVS project uses semianalytic models extensively, both to make testable predictions of the properties of SERVS galaxies and to inform our follow-up strategies in wavebands other than the near-infrared (e.g. Fig. 16). Two different semianalytic models are currently being used.

The first set is based on the Guo et al. (2011) version of the Munich semianalytic model for which light cones[57] were created and fully described in Henriques et al. (2012). The light cones contain a wide range of photometric bands that cover the

[57] These light cones are publicly available at http://www.mpa-garching.mpg.de/millennium.
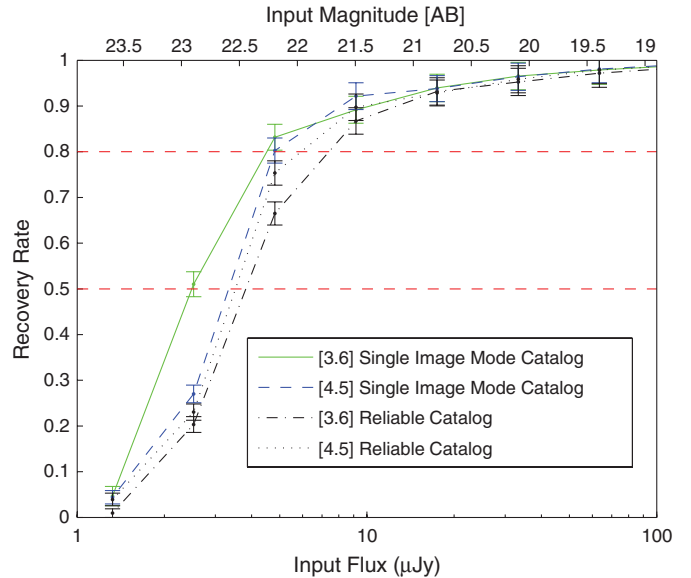

FIG. 15.—Completeness plots for Lockman Hole at [3.6] shown in green, [4.5] shown in blue, and the reliable dual-band detection catalogs shown in black. Using the techniques of Chary et al. (2004) and Lacy et al. (2005), model galaxies were simulated and placed in the mosaics. The sources were extracted using the same pipeline as the catalogs and the completeness was estimated as the recovery rate of the simulated model galaxies.

UV-to-NIR region of the spectra and allow an exact match to the observed selection criteria. They also include a choice between fluxes computed using the Bruzual & Charlot (2003) or the Maraston (2005) stellar populations. The latest have been shown to reconcile the predicted K-band rest-frame luminosity
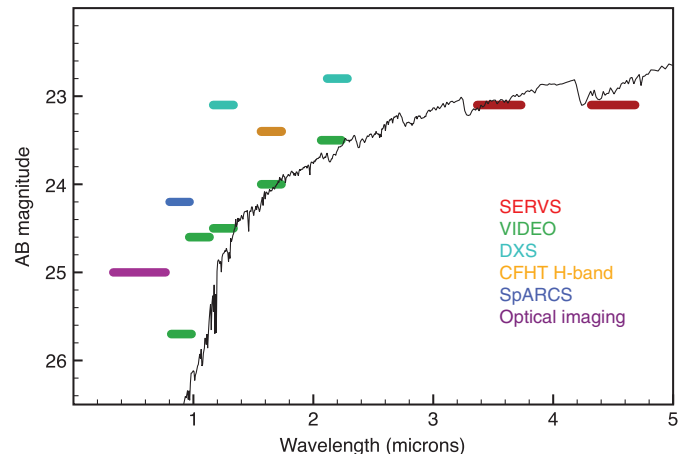

FIG. 16.—Approximate 5σ depths of SERVS and near-IR and optical surveys covering the same areas. Overplotted is the SED of a 1 Gyr old stellar population at $z = 2$ from Maraston (2005) for SERVS (*red solid lines*), VIDEO (*green solid lines*), DXS (*cyan solid lines*), CFHT H band (*orange solid lines*), and SpARCS (*blue solid lines*). Our target depth for optical-band imaging is shown as the magenta bar (several fields already have imaging to at least this depth). Note that no ground-based survey covers the entirety of the SERVS data; hence, multiple surveys are overlaid.

function with observations at high redshift (Henriques et al. 2011, 2012), for which IRAC data—such as those obtained with SERVS—have been essential. The second set, from van Kampen et al. (2012a, in preparation), includes both the effects of halo-halo and galaxy-galaxy mergers and uses GRASIL (Silva et al. 1998) to predict spectral energy distributions (SEDs) from the optical to submillimeter.

The expected redshift distribution is derived from the simulations and shown in Figure 17. A lower flux limit of 2 μJy (AB magnitude of $m_{[3.6]} < 23.1$) for the SERVS survey was used here. The expected redshift distribution of the SERVS galaxies peaks around $z \sim 1$ and extends to redshifts of $z \sim 3$, with a small fraction of objects detected up to $z \sim 4$. (For basic comparison purposes, the SWIRE photometric redshift distribution can be found in Rowan-Robinson et al. [2008]; at the current time, the SERVS photometric redshift distribution has not been derived, but will be presented by Pforr et al. [2012b, in preparation], as discussed in § 5.7.) Galaxies detected in SERVS will therefore span the epochs where galaxies gain the vast majority of their stellar mass. Indeed, Brown et al. (2007) and Cool et al. (2008) estimate that L^* galaxies roughly double in mass between $z = 0$ and $z \approx 1$. In addition, van Dokkum et al. (2010) recently showed that about half the mass of any given large galaxy is added between $z = 0$ and $z = 2$, by comparing galaxy samples at constant number densities. SERVS will be able to extend such studies out to higher redshifts with good statistics.

In order to roughly estimate the luminosity of the faintest galaxy SERVS will be able to detect in the IRAC [3.6] band as a function of redshift, three model SEDs were used: a starburst similar to M82, a 250 Myr stellar population, and a

5 Gyr stellar population from Maraston (2005). Figure 18 shows the luminosity of the faintest detectable source from 0.1 μm to 1 mm as a function of redshift, if this source was represented by one of the three SED models we used. SERVS might be able to detect L^* galaxies up to $z \sim 4$ and $0.1L^*$ out to $z \sim 1$. The luminosities of the Maraston SEDs can easily be converted to stellar masses by multiplying the luminosity of the 5 Gyr and 250 Myr stellar population models by 1.15865 and 0.00133, respectively. SERVS will ensure the derivation of robust stellar masses, because it includes the rest-frame near-infrared out to high redshifts. This coverage is essential to break the degeneracy between star formation history and dust reddening (Maraston et al. 2006). Photometric redshifts for SERVS galaxies are also being derived (see § 5.7).

5. ANCILLARY DATA

Overlaps with existing surveys in progress are listed in Table 8. Here, we provide a more detailed description of some of the most significant (in terms of their overlaps with SERVS) of these surveys.
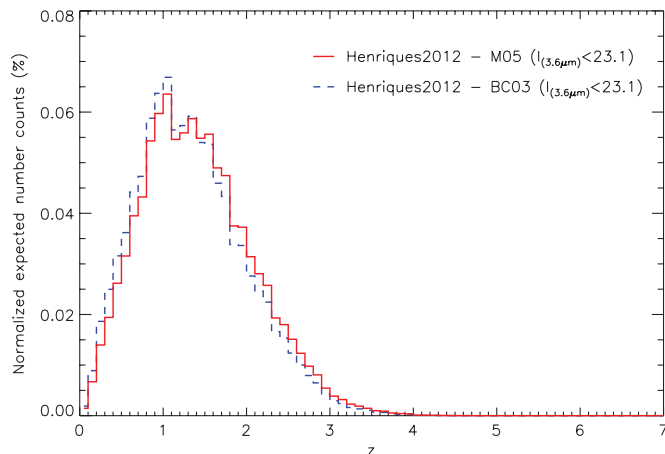

FIG. 18.—*Top*: SERVS faintest galaxy to be detected, in units of solar luminosities (integrated luminosity from the optical to the far-IR: 0.1 μm–1 mm) at a given redshift. *Bottom*: The three SED models considered here, consisting of an M82-like starburst galaxy (*blue solid lines*), a 250 Myr stellar population (*magenta solid lines*), and a 5 Gyr stellar population (*red solid lines*), scaled to the same 3.6 μm rest frame. SERVS can detect L^* galaxies out to $z \sim 4$, and $0.1L^*$ galaxies out to $z \sim 1$. At a redshift of 5, a starburst galaxy of luminosity $\sim 10^{12}$ $L_\odot$ could potentially be detected.

FIG. 17.—SERVS-expected normalized galaxy counts at the detection limit of 2 μJy (or $m_{[3.6]} < 23.1$). The two histograms correspond to flux limits applied to the [3.6] band either using the Maraston (2005) or Bruzual & Charlot (2003) stellar population models (see § 4.3).
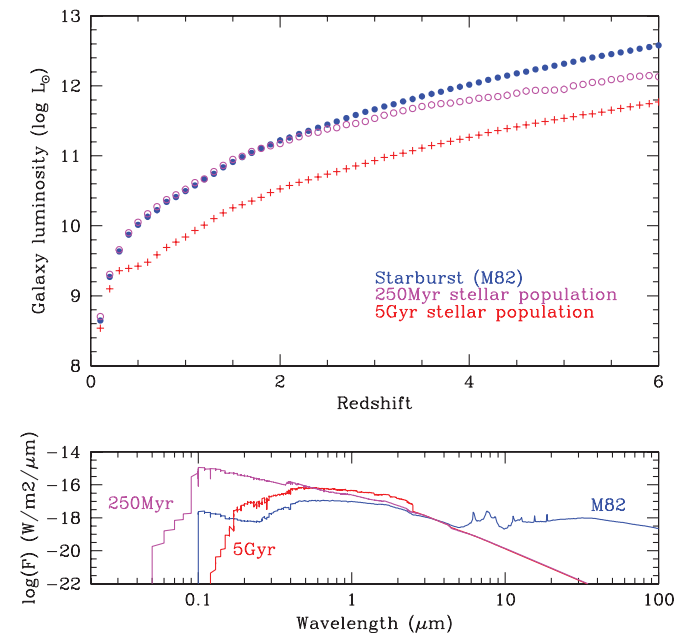
TABLE 8
SURVEYS AT OTHER WAVELENGTHS COVERING ≳10% OF SERVS FIELD (ALL-SKY SURVEYS EXCEPTED)

Field name	X-ray data	Optical data	Near-IR data	Mid-IR data	Far-IR/ submm data	Radio data
EN1	N04 (1)	SWIRE/INT (2), SDSS (3), SpARCS (4)	DXS (5)	SWIRE (6)	HerMES L5 (7), S2CLS (8)	G08a (9), Gr10 (10)
ES1	F08 (11)	ESIS (12), VOICE (13), SpARCS (4)	VIDEO (14)	SWIRE (6)	HerMES L6 (7)	ATLAS (15)
Lockman	W09 (16)	SWIRE/KPNO+ INT (2), SDSS (3), SpARCS (4)	DXS (5)	SWIRE (6)	HerMES L3, L5 (7), S2CLS (8)	OM08 (17), G08b (18), G10 (19), I09 (20)
CDFS	CDFS (21)	SWIRE/ CTIO (22), GaBoDS (23), VVDS (24), VOICE (13), SpARCS (4)	VIDEO (14)	SWIRE (6), SIMPLE (25)	HerMES L2, L5 (7), LABOCA/ LESS (26)	ATLAS (15), M08 (27)
XMM-LSS	XMM-LSS (28), SXDS (29)	CFHTLS (30), VVDS (24), SXDS (34)	VVDS (31), UDS (5), VIDEO (14), DXS (5)	SWIRE (6), SpUDS (25)	HerMES L5 (7), S2CLS (8)	VVDS-VLA (32), S06 (33)

REFERENCES.—(1) *Chandra* proposal 6900602 (PI Nandra); (2) González-Solares et al. 2011; (3) Abazajian et al. 2009; (4) DeGroot et al. 2012, in preparation; (5) Lawrence et al. 2007; (6) Lonsdale et al. 2003 and Surace et al. 2005; (7) Oliver et al. 2012; (8)http://www.jach.hawaii.edu/ JCMT/surveys/Cosmology.html; (9) Garn et al. 2008a; (10) Grant et al. 2010; (11) Feruglio et al. 2008; (12) Berta et al. 2006, 2008; (13) PIs G. Covone and M. Vaccari, http://people.na.infn.it/ covone/voice/voice.html; (14) Jarvis et al. 2012, in preparation; (15) Norris et al. 2006 and Middelberg et al. 2008; (16) Wilkes et al. 2009; (17) Owen & Morrison 2008; (18) Garn et al. 2008b; (19) Garn et al. 2010; (20) Ibar et al. 2009; (21) Lehmer et al. 2005; (22) http://www.astro.caltech.edu/~bsiana/cdfs opt; (23) Garching-Bochum Deep Survey, Hildebrandt et al. 2006; (24) Le Fèvre et al. 2005; (25) Damen et al. (2009), irsa.ipac.caltech.edu/data/SPITZER/docs/spitzermission/observingprograms/legacy/; (26) Survey of the CDFS with the Large Apex Bolometer Camera (LABOCA), Weiß et al. (2009); (27) Miller et al. 2008; (28) Pierre et al. 2007; (29) Ueda et al. 2008; (30) www.cfht.hawaii.edu/Science/CFHTLS; (31) Iovino et al. 2005 and Temporin et al. 2008; (32) Bondi et al. 2007; (33) Simpson et al. 2006; (34) Furusawa et al. 2008.

5.1. Optical Surveys

A number of optical surveys overlap one or more of the SERVS fields. Among the most significant are the ESO/Spitzer Imaging Survey (ESIS) in ES1 (Berta et al. 2006, 2008), which reaches depths of 25, 25, 24.5, and 23.2 (Vega) in B, V, R, and I, respectively; the CFHTLS (both deep and wide pointings in u^*, g, r,i, and z in the XMM-LSS field reaching depths of 28.7, 28.9, 28.5, 28.4, and 27.0 and 26.4, 26.6, 25.9, 25.5, and 24.8 AB magnitudes, respectively); and ancillary SWIRE data in Lockman, EN1, and CDFS in a variety of depths and filters, but typically reaching at least $r = 24.5$ (Gonzalez-Solares et al. 2011).

The Spitzer Adaptation of the Red Sequence Cluster Survey (SpARCS;[58] Muzzin et al. 2009, 2012a, in preparation; Wilson et al. 2009; DeGroot et al. 2012) has imaged the entire SWIRE area (excluding the XMM-LSS field, which is covered by the CFHTLS) in the z' filter using MegaCam on the Canada-France-Hawaii Telescope or the mosaic camera on the Blanco

Telescope at Cerro Tololo Inter-American Observatory (CTIO). The MegaCam observations reach a mean depth of 24.2 AB magnitudes, and the mosaic camera observations reach a mean depth of 24.0 AB magnitudes. The SpARCS collaboration has spectroscopically confirmed ~15 clusters at $z \gtrsim 1$ (Muzzin et al. 2009, 2011, 2012b, in preparation; Wilson et al. 2009, Wilson et al., 2012a, in preparation; Demarco et al. 2010) and is in the process of carrying out detailed multipassband and spectroscopic follow-up studies (Rettura et al. 2012, in preparation; Lidman et al. 2012, in preparation; Noble et al. 2012, in preparation; Ellingson et al. 2012, in preparation; Wilson et al. 2012b, in preparation).

Started in October 2011, the VST/VOICE survey (PIs G. Covone and M. Vaccari) is surveying the CDFS and ES1 fields in u, g, r, and i, aiming at reaching AB ~ 26 at 5σ.

Optical spectroscopy has thus far been confined to small regions of SERVS—such as the recently completed PRIMUS (PRism MUlti-object survey; Coil et al. 2011) project, covering parts of the ES1, CDFS, and XMM-LSS fields—or to specific types of objects. The largest spectroscopic survey is the VIMOS-VLT Deep Survey (VVDS; Le Fèvre et al. 2005),

---

[58] See http://www.faculty.ucr.edu/~gillianw/SpARCS.

which has $\approx 10,000$ spectroscopic redshifts for field galaxies with $17.5 < I_{AB} < 24$ in their XMM-LSS and CDFS subfields (Le Fèvre et al. 2005). In addition, spectra of active galactic nuclei (AGNs) and quasars, now totaling several hundred objects selected by various techniques, have been obtained in the SERVS fields by Lacy et al. (2007, 2012, in preparation) and Trichas et al. (2010).

5.2. Ground-based Near-Infrared Surveys

One of several major surveys to be carried out by the Visible and Infrared Survey Telescope for Astronomy (VISTA) is the five filter near-infrared VIDEO survey (Jarvis et al. 2012, in preparation), which will cover 12 deg^2 to AB magnitudes of 25.7, 24.6, 24.5, 24.0, and 23.5 in Z, Y, J, H, and K_s filters. The ES1, XMM-LSS, and CDFS SERVS fields are designed to exactly overlap their corresponding VIDEO fields. The combination of VIDEO and SERVS will be a particularly potent tool for the study of galaxy evolution at high redshifts.

The Deep Extragalactic Survey (DXS) is part of UKIDSS (Lawrence et al. 2007) and will cover the Lockman and EN1 fields to 23.1 and 22.5 (AB) in J and K, respectively. As of October 2011, Data Release 7 is available to the entire astronomical community. It covers parts of the EN1, Lockman, and XMM-LSS fields. Data Release 9 is available to the community served by the European Southern Observatory, and it includes additional data.

5.3. Mid- and Far-Infrared and Submillimeter Surveys

The SERVS fields were designed to be contained within the SWIRE fields. This has mostly been achieved, although constraints from other surveys mean that a small fraction of SERVS lies outside of the SWIRE coverage.

The HerMES[59] survey is a Herschel Key Project to survey most of the extragalactic *Spitzer* fields, including the SWIRE fields. HerMES has six levels, corresponding to increasing depths, with level 6 being the shallowest. Smith et al. (2012) give measured flux densities at which 50% of injected sources result in good detections at the SPIRE wavelengths of 250, 350, and 500 μm, ranging from 11.6, 13.2, and 13.1 mJy to 25.7, 27.1, and 35.8 mJy, depending on the depth of the observation, with the deeper observations being confusion-limited. All of SERVS is covered to level 6 or deeper, with significant areas as deep as level 3 (5σ limiting flux density ≈ 7 mJy at 160 μm with the Photodetector Array Camera & Spectrometer (PACS) instrument). Full details of the HerMES survey are given in Oliver et al. (2012).

The wide-area component of the SCUBA-2 Cosmology Survey (S2CLS) will cover the XMM-LSS, Lockman, EN1, and

---

[59] See http://hermes.sussex.ac.uk/.

CDFS fields. The survey will be performed at 850 μm to a root mean square (rms) noise of 0.7 mJy.

5.4. Radio Surveys

The Australia Telescope Large Area Survey (ATLAS; Norris et al. 2006) overlaps with much of the SERVS fields in ES1 and CDFS. The ATLAS survey will have an rms of 10 μJy and a spatial resolution of $\approx 8''$ at 1.4 GHz across both fields (Banfield et al. 2012, in preparation). A preliminary release of the survey data for CDFS (Norris et al. 2006) and ES1 (Middelberg et al. 2008) has an rms noise of 30 μJy. An image showing the overlap between the SERVS and ATLAS fields can be found in the accompanying article by Norris et al. (2011a). Subsequent ATLAS data releases will be published shortly by Hales et al. (2012, in preparation) and Banfield et al. (2012, in preparation).

The EN1 and Lockman fields have been surveyed at 610 MHz with the Giant Meter Wave Telescope (GMRT; Garn et al. 2008a, 2008b, respectively). These surveys have a mean rms of ≈ 60 μJy at a spatial resolution of $\approx 6''$.

The Very Large Array (VLA) has conducted several surveys in the SERVS fields. The Lockman field includes the deepest radio survey at 1.4 GHz to date, a single $40' \times 40'$ pointing centered at 161.5 days, $+59.017$ days, reaching a 5σ detection limit of 15 μJy near the center of the primary beam (Owen & Morrison 2008) and further deep coverage by Ibar et al. (2009). Simpson et al. (2006) have surveyed the Subaru Extragalactic Deep Survey region with the VLA to a detection limit of 100 μJy, and Bondi et al. (2007) have surveyed the VVDS field in XMM-LSS at both 610 MHz with the GMRT and 1.4 GHz with the VLA to limits of ≈ 200 and 80 μJy, respectively. The Faint Images of the Radio Sky at Twenty cm (FIRST; White et al. 1997) survey covers the Lockman and EN1 surveys and part of the XMM-LSS survey at 1.4 GHz to a sensitivity limit of ≈ 1 mJy at a spatial resolution of $\approx 5''$.

Two pathfinder telescopes for the proposed Square Kilometer Array are currently under construction in the southern hemisphere. Both of these telescopes will undertake continuum surveys that will cover the southern SERVS fields. The Evolutionary Map of the Universe (EMU; Norris et al. 2011b) survey with the Australian Square Kilometer Array Pathfinder (AS-KAP) will cover the whole southern sky to 10 μJy rms sensitivity at 1.4 GHz with a $10''$ FWHM (full width at half-maximum) synthesized beam. The South African Karoo Array Telescope (MeerKAT; Jonas 2009) will conduct the MeerKAT International Giga-Hertz Tiered Extragalactic Exploration (MIGHTEE) survey, which has a strong SERVS participation. MIGHTEE has several tiers, one of which will include the southern SERVS/VIDEO fields to 1 μJy rms at 1.4 GHz with an $\approx 5''$ FWHM beam. In the north, the Low Frequency Array (LOFAR; Röttgering et al. 2011) will target the SERVS/SWIRE fields for deep surveys at frequencies of ~100 MHz. In the northern hemisphere, the WODAN (Westerbork Observations of the Deep APERTIF Northern-Sky) is being proposed for

Westerbork+APERTIF and will match EMU sensitivity and re-solution (Röttgering et al. 2011).

5.5. X-Ray Surveys

The XMM-LSS field overlaps with the XMM-LSS survey (Pierre et al. 2007) and the Subaru/XMM-Newton Deep Survey (SXDS; Ueda et al. 2008). Wilkes et al. (2009) have a deep *Chandra* survey overlapping with the deep VLA pointing of Owen & Morrison (2008) in Lockman. In EN1, *Chandra* program 690062 (PI Nandra) covers ≈ 1 deg^2 of the central portion of the field.

5.6. Further Ground-based Data Taken or to be Taken by the SERVS Team

Further multiwavelength ancillary data on the SERVS fields are currently being obtained with the overall goal of matching the SERVS depth in shorter wavebands. These data will be made available as part of the overall SERVS public release. Observations are concentrated on longer optical and near-IR wavebands, as these are generally more useful for photometric redshift estimates at higher redshifts (van Dokkum et al. 2006; Brammer et al. 2008; Ilbert et al. 2009; Cardamone et al. 2010). In the optical, the SDSS filter set is used where possible, as the
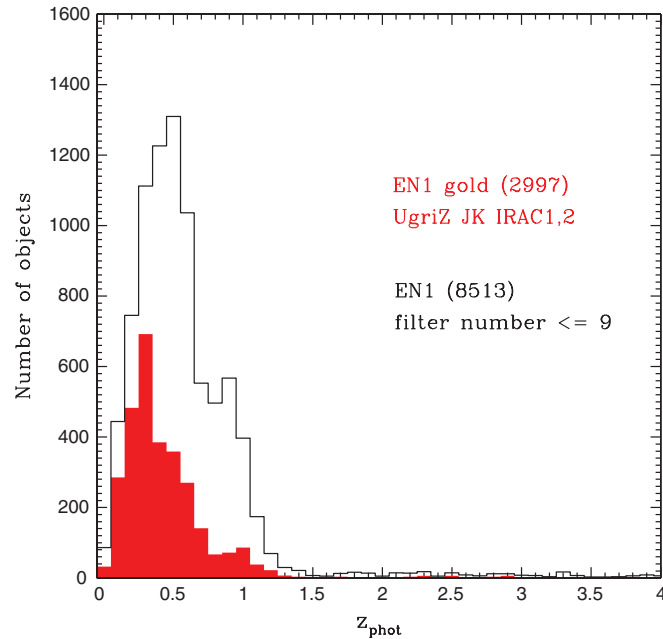

FIG. 19.—Photometric redshift distribution of SERVS galaxies in EN1 (*black histogram*). Photometric redshifts are obtained from SED fitting using the HyperZ code and the Maraston (2005) stellar population synthesis templates. Included are only objects classified as extended in the optical and near-IR bands in order to exclude stars and AGN-dominated sources. Additionally the *red histogram* shows the subsample of sources which are detected in all filter bands (, , , , , , , IRAC1, IRAC2 for EN1) which provides the most robust photometric redshift estimates. From Pforr, Maraston & Tonini (2012b, in prep.).

narrower bands allow higher-fidelity photometric redshifts than the Johnson-Cousins system (see Fig. 19).

Target depth in the optical is an AB magnitude ≈ 25 and ≈ 23 in the near-infrared (the area covered by VIDEO will be significantly deeper than this). Figure 16 shows a comparison of the SERVS depth with those of the other major optical/near-IR surveys planned or in progress.

Observations with SuprimeCam on the Subaru telescope have been carried out in i and z bands as part of the Gemini-Subaru (PI A. Verma) and Keck-Subaru (PI S.A. Stanford) time swaps. The z-band observations are concentrated in the northern fields, as VIDEO will cover the southern fields in Z.

An optical imaging campaign of the ES1 and CDFS fields using the CTIO 4 m mosaic camera has been completed (in November 2009 and October 2010, with a total of nine nights). The specific goals were (1) to complete imaging in r and i to 24.2 and 23.2 (Vega) over the whole area of the ES1 and CDFS fields and (2) to obtain deeper r- and i-band data (to 25.0 and 24.0) in the center of ES1 to complement deep surveys by VISTA and warm *Spitzer*, and where deep data at shorter wavelengths exist from ESO. Images are currently being processed.

An H-band imaging campaign, led by M. Lehnert, has obtained H-band data with WIRCAM on the CFHT, to match the UKIDSS DXS J and K imaging in the EN1 field. These data are currently being analyzed.

5.7. Photometric Redshifts

The wealth of ground-based data available in the SERVS fields in conjunction with the IRAC data obtained through the SERVS project provides the ideal basis for a robust determination of photometric redshifts, stellar masses, and other stellar population properties from SED fitting. Here, the photometric redshifts were computed via SED fitting using the HyperZ code (Bolzonella et al. 2000) and the Maraston (2005) stellar population templates, following the procedure outlined in Pforr et al. (2012b, in preparation). In brief, the best fit is determined by minimizing the χ^2 between a large grid of population model templates (for various star formation histories, ages, metallicities, reddening, and redshifts) and the photometric data. Specifically, we use a template set with exponentially declining star formation rates, metallicities ranging from $1/5$ to twice solar, a minimum age of 0.1 Gyr, and a Calzetti et al. (2000) reddening law with extinction parameter A_V ranging between 0 and 3 mag. This template set gives the minimum variance between the derived photometric redshifts and the spectroscopic redshift calibration set.

By comparing with available spectroscopic redshifts using the compilation of redshifts in the SWIRE fields by Vaccari et al. (2012, in preparation), a redshift accuracy of $\Delta z/(1 + z) = 0.011 \pm 0.072$ is obtained for a data set with an optimal wavelength coverage (i.e., U, g, r, i, Z, J, K, IRAC1 [3.6], and

IRAC2 [4.5] for the EN1 field). Due to the small[60] number of SERVS objects with available spectroscopic redshifts, we further confirmed the redshift accuracy by cross-matching the VVDS survey in the extended Chandra Deep Field (Le Fèvre et al. 2005) with the IRAC SIMPLE survey (Damen et al. 2009), obtaining 831 matches with redshifts and 4.5 μm fluxes greater than 3 μJy. However, the diversity inherent to the ancillary data coverage for the SERVS fields impairs the redshift determination, particularly for objects with a narrower wavelength coverage. This is explored in detail in Pforr et al. (2012b, in preparation). In summary, photometric redshifts display larger scatter when the wavelength coverage used for the fitting is narrow, i.e., does not incorporate the rest-frame UV, optical or near-IR rest-frame or a combination thereof, particularly when spectral breaks such as the 4000 Å break and the Lyman break are not covered by the filter setup (see Ilbert et al. 2009 and Bolzonella et al. (2000) for studies on photometric redshift accuracies).

The distribution of photometric redshifts obtained for extended[61] objects, i.e., galaxies, in EN1 is shown in Figure 19. The red histogram highlights the most robust sample (so-called gold sample) with the best wavelength coverage, i.e., corresponding to the case where the object is detected in all filter bands. The black histogram also includes objects that were detected in less photometric bands.

6. ONGOING SCIENCE WITH SERVS

In this section, we summarize already-published or ongoing work by SERVS team members to underline some of the key science goals of the SERVS survey.

6.1. Galaxies and Their Environments

Sampling ~0.8 Gpc^3, SERVS is large enough to contain significant numbers of objects while still being deep enough to find L^* galaxies out to $z \approx 4$ (Fig. 17). By combining the five different fields of SERVS, the survey effectively averages over large-scale structure and is able to present a true picture of the average properties of galaxies in the high-redshift universe.

Galaxy-galaxy correlations are being computed by van Kampen et al. (2012b, in preparation) in the SERVS fields. The five large, well-separated, SERVS fields enable us to average-out the effects of large-scale structure on such measurements. Initial results on the EN1 field show the evolution of

the correlation function between high redshifts ($z > 1.3$) and intermediate redshifts (~0.8) using simple [3.6]–[4.5] color cuts.

SERVS is deep enough and wide enough to find field clusters at $z > 2$, should they exist in significant numbers. The SERVS fields lie within the SpARCS fields (see survey description in § 5.1; DeGroot et al. 2012, in preparation), The deep SERVS observations will allow both a more accurate measurement of the faint end of the luminosity function of known SpARCS clusters that fall within the SERVS footprint and also the detection of new clusters at higher redshifts than are possible with SpARCS.

In addition, Geach et al. (2012, in preparation) are pursuing a cluster selection technique using photometric redshifts combined with Voronoi tessellation in an attempt to identify further, mostly lower-mass, cluster candidates.

6.2. The Active Galactic Nuclei Engine

The [3.6] and [4.5] bands are important diagnostics of AGN SEDs, as they are where host-galaxy light and hot dust emission from the torus overlap in the SEDs of many dust-obscured AGNs and quasars at moderate redshifts ($z \sim 1$). In unobscured, or lightly obscured, objects, this is where the optical/UV emission from the accretion disk transitions to the hot dust emission. Petric (2010) and Petric et al. (2012, in preparation) present SEDs of AGNs and quasars selected in the midinfrared and use SERVS data to help apportion the different sources of near-infrared light. The luminosities of the hosts themselves, if free from contamination by AGN-related light, can also be used to study the stellar masses of the host galaxies.

6.3. AGNs and Their Environments

Current models for galaxy formation indicate that AGNs and quasar activity play an important role in galaxy formation (e.g., Hopkins et al. 2006), regulating the growth of their host galaxies through feedback (see, for example, Schawinski et al. [2007] or, more recently, Farrah et al. [2012], who provide new and strong evidence for AGN feedback). However, the exact nature of this feedback process is unclear. Environments in which AGNs and quasars lie can indicate the masses of the dark halos they inhabit and also how these masses depend on AGN luminosity and redshift (Farrah et al. 2004). These can illuminate models for feedback; for example, a preponderance of AGNs in massive halos, accreting at relatively low rates, might be an indicator that their host galaxies are no longer growing rapidly (Hopkins et al. 2007). At low redshifts ($z < 0.6$) the SDSS has been used to successfully perform these experiments (Padmanabhan et al. 2009). SERVS is able to take these studies to $z \gg 1$.

One particular area where SERVS is uniquely valuable is in determining the environments of high-redshift AGNs. Falder

---

[60] In the EN1 field, among the 2997 extended sources with optimal wavelength coverage (respectively, 8513 with nonoptimal wavelength coverage), only 30 (respectively, 60) have spectroscopic redshifts.

[61] The decision as to whether an object is extended is based on stellarity flags provided with the ancillary data in optical and near-IR filter bands. Sources with a pointlike nature indicative of stars or AGNs were excluded, since the model template we use in the fitting does not include nonthermal emission.
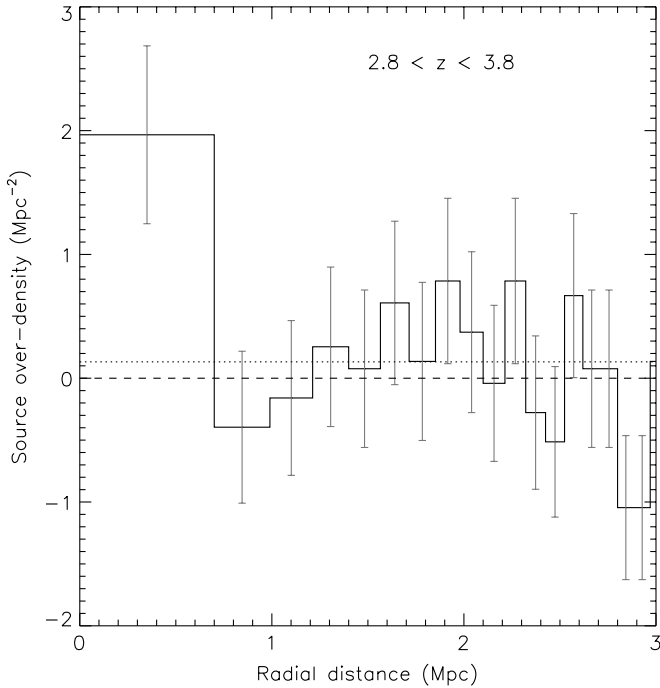
FIG. 20.—Stacked source over-density vs radial distance for the 11 QSOs in the redshift range of . The first bin has a radius of 700 kpc and the other bins are of the same area as the first. The error bars show the Poisson error on the number counts. The dashed line shows the subtracted local background level (zero level) determined from an annulus of (400″) from the QSOs. The dotted line shows, for comparison, the global background as determined from taking the average source density in large apertures over the SERVS fields. This is the source density before being corrected for completeness. Figure from Falder et al. (2011).

et al. (2011) find significant ($>4\sigma$) overdensity of galaxies around QSOs in a redshift bin centered on $z \sim 2.0$ and an ($>2\sigma$) overdensity of galaxies around QSOs in a redshift bin centered on $z \sim 3.3$ (see Fig. 20).

Nielsen et al. (2012, in preparation) are investigating the environments of AGNs and quasars selected in the midinfrared. For the first time, the environments of luminous quasars at $0.8 < z \lesssim 3$ are being characterized, enabling a comparison of the environments of dust-obscured and normal quasars at these redshifts.

6.4. High-z Quasar Searches

The unique multiband SERVS data set will be a valuable tool for constraining the faint end of the quasar luminosity function at high redshifts. Quasar searches have been, or will be, carried out in the SERVS fields using the combination of SERVS, DXS, VIDEO, and SpARCS data, in addition to the SERVS CTIO and Subaru ancillary data. This large range of wavelengths allows for the rejection of many contaminants of high-z quasar searches on the basis of near-infrared photometry alone. Current estimates of the high-z quasar luminosity function (e.g., Willott

et al. 2010) suggests somewhere between 3–14 quasars at $5.5 < z < 6.5$ and 1–5 quasars at $6.5 < z < 7.5$. The large range is due to the uncertainty in the faint-end slope of the quasar luminosity function, and SERVS will be able to constrain this well.

6.5. Infrared-Faint Radio Sources

Norris et al. (2006) describe the discovery of infrared-faint radio sources, a population of radio sources with host-galaxy fluxes well below the limit of the SWIRE survey. Huynh et al. (2010) used deep IRAC data to place even more stringent limits on them and concluded that these are most likely radio-loud AGNs with faint host galaxies, but the sample to date is small. Norris et al. (2011a) present an initial study of this hitherto-unsuspected population with SERVS, including stacking of objects that are too faint to be detected, even in SERVS, and that may represent very high redshift radio-loud galaxies, possibly suffering from significant dust extinction (see Fig. 21).

Using a combination of SERVS data and GMRT/VLA radio observations of the Lockman Hole at 610 MHz and 1.4 GHz, Afonso et al. (2011) study a sample of Ultra Steep Spectrum (USS) radio sources and suggest the likely existence of higher redshifts among the submillijansky USS population, raising the possibility that the high efficiency of the USS technique for the selection of high-redshift sources remains even at the submillijansky level.

6.6. Obscured Star Formation

Although SERVS cannot be used as a direct indicator of obscured star formation on its own, overlap with surveys by SCUBA-2 (S2CLS) and *Herschel* (HerMES) will allow more reliable source identification than is possible using shorter-wavelength data and better characterization of any extinction of the stellar light, as well as the stellar mass of the galaxy. Based on recent simulations of *Herschel* observations, we expect to detect $\sim$700 unconfused sources per deg^2 in $\geq$3 *Herschel* bands (Fernandez-Conde et al. 2008). At the SERVS depths, we expect to detect more than 95% of these sources in both IRAC bands and, with the aid of our ancillary optical and near-infrared data, to thus obtain photometric redshifts and stellar masses for $\sim$12,000 sources. This will be sufficient to study trends in star formation rate with stellar mass and redshift: for example, to test the idea of "downsizing" of the most actively star-forming galaxies.

7. SUMMARY

The *Spitzer* Extragalactic Representative Survey (SERVS) is designed to open up a medium-depth, medium-area part of parameter space in the near-infrared, covering 18 deg^2 to $\approx$2 μJy in the *Spitzer* [3.6] and [4.5] bands in five highly observed astronomical fields (EN1, ES1, Lockman Hole, CDFS,
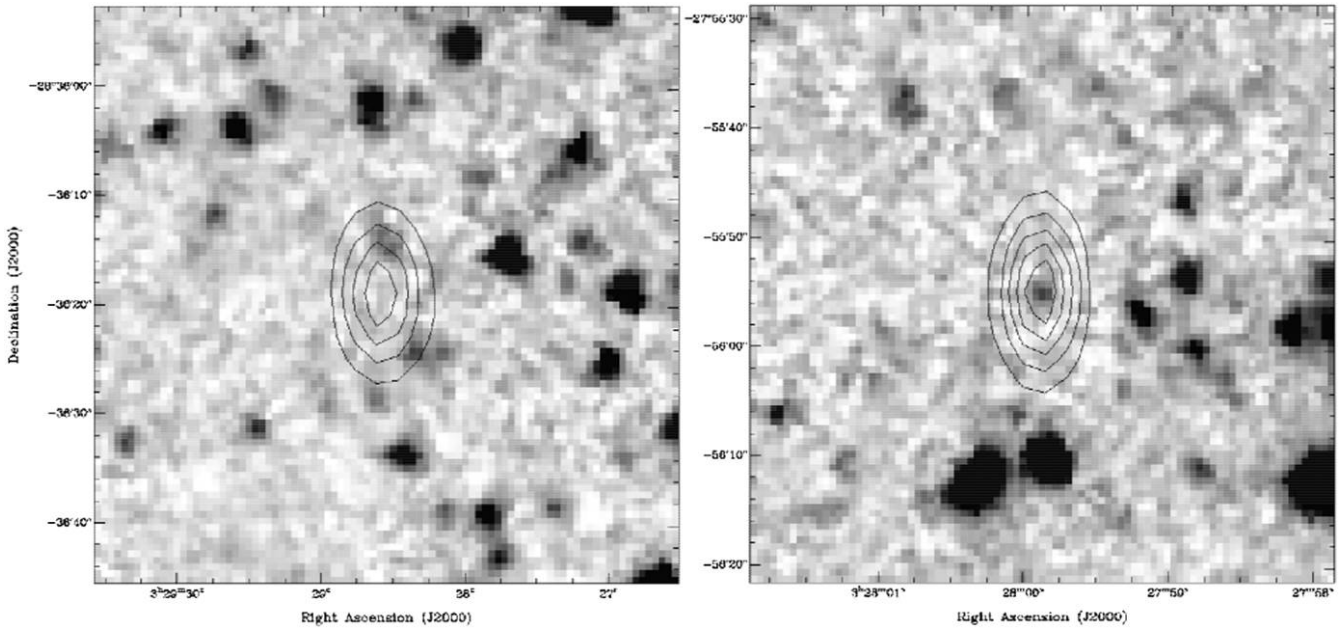
FIG. 21.—Two representative infrared-faint radio sources (IFRS). The greyscale is the [3.6] SERVS data, and the contours are the 20 cm image, with contour levels of (1, 2, 3, 4, 5) mJy/beam. The left hand image is a non-detection (CS0194) and the right-hand image is a candidate detection (CS0114), Figure 2. of Norris et al. (2011a).

and XMM-LSS). The five SERVS fields are centered on, or close to, those of corresponding fields surveyed by the shallower SWIRE fields, and they overlap with several other major surveys covering wavelengths from the X-ray to the radio. Of particular importance are near-infrared data, as these allow accurate photometric redshifts to be obtained. SERVS overlaps exactly with the 12 deg^2 of the VISTA VIDEO survey in the south and is covered by the UKIDSS DXS survey in the north. SERVS also has good overlap with HerMES in the far-infrared, which covers SWIRE and other *Spitzer* survey fields, with deeper subfields within many of the SERVS fields. Sampling $\sim$0.8 Gpc^3 and redshifts from 1 to 5, the survey is large enough to contain significant numbers of rare objects (such as luminous quasars, ultraluminous infrared galaxies, radio galaxies, and galaxy clusters), while still being deep enough to find L^* galaxies out to $z \approx 4$. In this article, we have described the *Spitzer* observations, the data processing, and the wealth of ancillary data available in the fields covered by SERVS. Mosaics and catalogs will be made available to the community in the summer of 2012 through the Infrared Science Archive (IRSA).

APPENDIX A

NUMBER COUNTS FOR THE EN1, ES1, LOCKMAN, AND CDFS FIELDS

Number counts were derived for the five fields. Source colors were also compared with 2MASS (see details in § 4.2). We present here the four remaining fields: EN1, ES1 (top and bottom panels of Fig. 22), Lockman, and CDFS (top and bottom panels of Fig. 23). All of them show consistent number count features and completeness levels. SERVS bright stars colors for all of the fields are coherent with 2MASS.
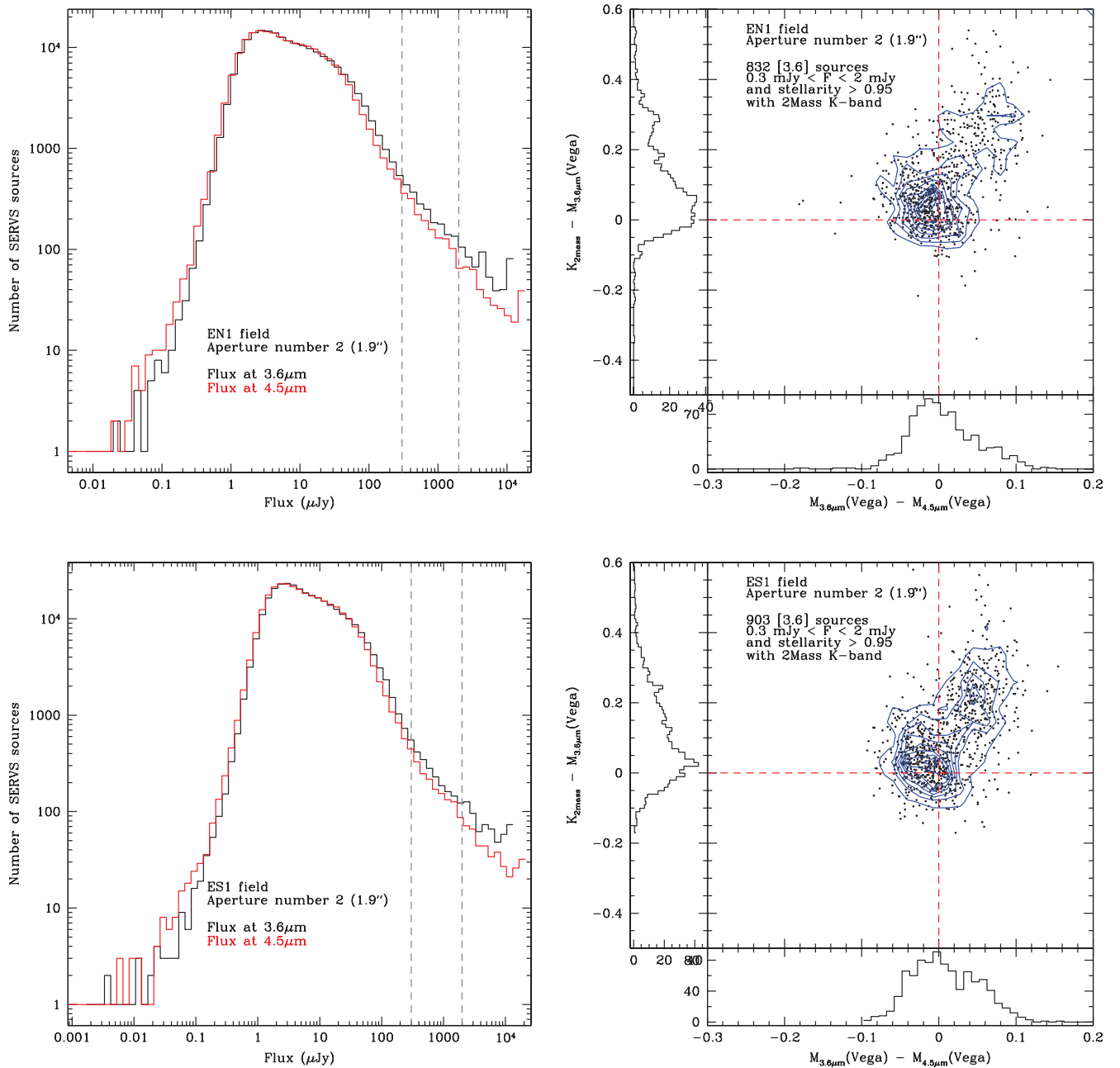
F_{IG}. 22.—*Left side*: SERVS number counts versus flux at [3.6] and [4.5] for the EN1 (*top*) and ES1 (*bottom*) fields. Grey dashed lines show the selection of sources used in the bottom plot (with fluxes as). *Right side*: Color-color plot showing (Vega) versus (Vega) for sources within the flux range defined by the grey dashed lines above, plus a cut in stellarity index and the existence of a 2MASS -band measurement as an additional constraint. *Red dashed* lines help pinpoint the location of the (0,0) point in this diagram.

APPENDIX B

SEXTRACTOR AND MOPEX PARAMETERS USED FOR THE IMAGE PROCESSING AND THE CATALOG EXTRACTION

Mopex was used to process and co-add the raw images and SExtractor to extract information on the sources within. In Table 8 we list the core parameters used in both.
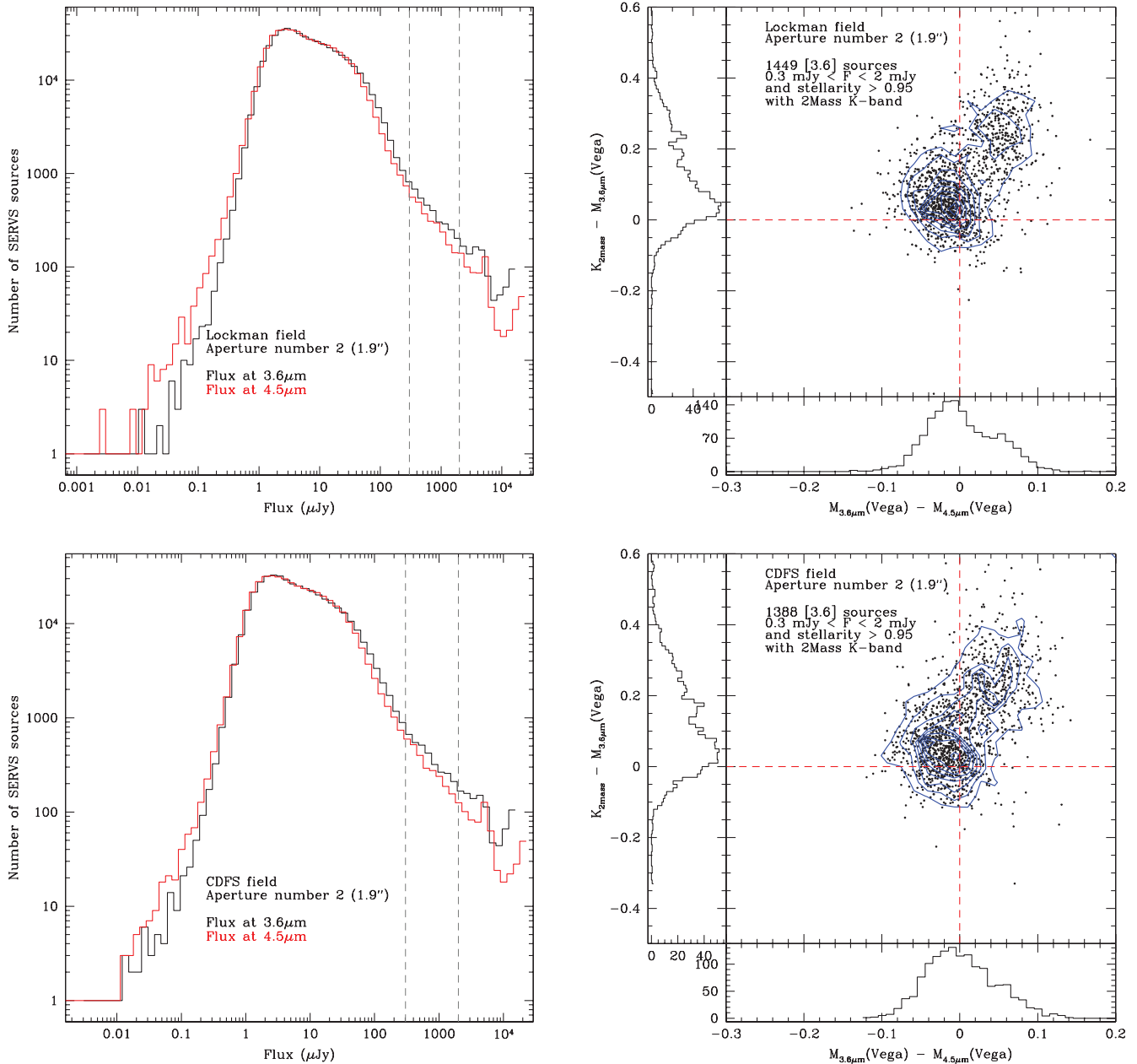
FIG. 23.—*Left side*: SERVS number counts versus flux at [3.6] and [4.5] for the Lockman (*top*) and CDFS (*bottom*) fields. Grey dashed lines show the selection of sources used in the bottom plot (with fluxes as). *Right side*: Color-color plot showing (Vega) versus (Vega) for sources within the flux range defined by the grey dashed lines above, plus a cut in stellarity index and the existence of a 2MASS -band measurement as an additional constraint. *Red dashed* lines help pinpoint the location of the (0,0) point in this diagram.

REFERENCES

Abazajian, K. N., et al. 2009, ApJS, 182, 543

Afonso, J., et al. 2011, http://adsabs.harvard.edu/abs/2011ApJ...743
..122A

Ashby, M. L. N., et al. 2009, ApJ, 701, 428

Berta, S., et al. 2006, A&A, 451, 881

———. 2008, A&A, 488, 533

Bertin, E., & Arnouts, S. 1996, A&AS, 117, 393

Bolzonella, M., Miralles, J.-M., & Pelló, R. 2000, A&A, 363, 476

Bondi, M., et al. 2007, A&A, 463, 519

Brammer, G. B., van Dokkum, P. G., & Coppi, P. 2008, ApJ, 686, 1503

Brown, M. J. I., Dey, A., Jannuzi, B. T., Brand, K., Benson, A. J.,
Brodwin, M., Croton, D. J., & Eisenhardt, P. R. 2007, ApJ, 654, 858

Bruzual, G., & Charlot, S. 2003, MNRAS, 344, 1000

Calzetti, D., Armus, L., Bohlin, R. C., Kinney, A. L., Koornneef, J., & Storchi-Bergmann, T. 2000, ApJ, 533, 682

Capak, P. L., et al. 2011, Nature, 470, 233

Cardamone, C. N., et al. 2010, ApJS, 189, 270

Chary, R., et al. 2004, ApJS, 154, 80

Cimatti, A., et al. 2008, A&A, 482, 21

Coil, A. L., et al. 2011, ApJ, 741, 8

Cool, R. J., et al. 2008, ApJ, 682, 919

Damen, M., Labbé, I., Franx, M., van Dokkum, P. G., Taylor, E. N., & Gawiser, E. J. 2009, ApJ, 690, 937

Demarco, R., et al. 2010, ApJ, 711, 1185

Dickinson, M., Giavalisco, M., & GOODS Team 2003, in The Mass of Galaxies at Low and High Redshift, ed. R. Bender, & A. Renzini (New York: Springer), 324

Falder, J. T., et al. 2011, ApJ, 735, 123

Farrah, D., Geach, J., Fox, M., Serjeant, S., Oliver, S., Verma, A., Kaviani, A., & Rowan-Robinson, M. 2004, MNRAS, 349, 518

Farrah, D., et al. 2012, ApJ, 745, 178

Fazio, G. G., et al. 2004, ApJS, 154, 10

Fernandez-Conde, N., Lagache, G., Puget, J.-L., & Dole, H. 2008, A&A, 481, 885

Feruglio, C., et al. 2008, A&A, 488, 417

Furusawa, H., et al. 2008, ApJS, 176, 1

Garn, T., Green, D. A., Riley, J. M., & Alexander, P. 2008a, MNRAS, 383, 75

———. 2008b, MNRAS, 387, 1037

Garn, T. S., Green, D. A., Riley, J. M., & Alexander, P. 2010, Bull. Astron. Soc. India, 38, 103

Glazebrook, K., Peacock, J. A., Collins, C. A., & Miller, L. 1994, MNRAS, 266, 65

Gonzalez-Solares, E. A., et al. 2011, MNRAS, 416, 927, http://adsabs.harvard.edu/abs/2011MNRAS.416..927G

Grant, J. K., Taylor, A. R., Stil, J. M., Landecker, T. L., Kothes, R., Ransom, R. R., & Scott, D. 2010, ApJ, 714, 1689

Grogin, N. A., et al. 2011, ApJS, 197, 35

Guo, Q., et al. 2011, MNRAS, 413, 101

Henriques, B., Maraston, C., Monaco, P., Fontanot, F., Menci, N., De Lucia, G., & Tonini, C. 2011, MNRAS, 415, 3571, http://adsabs.harvard.edu/abs/2011MNRAS.415.3571H

Henriques, et al. 2012, http://adsabs.harvard.edu/abs/2011MNRAS.415.3571H

Hildebrandt, H., et al. 2006, A&A, 452, 1121

Hopkins, P. F., Hernquist, L., Cox, T. J., Di Matteo, T., Robertson, B., & Springel, V. 2006, ApJS, 163, 1

Hopkins, P. F., Lidz, A., Hernquist, L., Coil, A. L., Myers, A. D., Cox, T. J., & Spergel, D. N. 2007, ApJ, 662, 110

Huynh, M. T., Norris, R. P., Siana, B., & Middelberg, E. 2010, ApJ, 710, 698

Ibar, E., Ivison, R. J., Biggs, A. D., Lal, D. V., Best, P. N., & Green, D. A. 2009, MNRAS, 397, 281

Ilbert, O., et al. 2006, A&A, 453, 809

———. 2009, ApJ, 690, 1236

Iovino, A., et al. 2005, A&A, 442, 423

Jonas, J. 2009, in Proc. IEEE, 97, 1522

Koekemoer, A. M.,et al. 2011, ApJS, 36, 197

Lacy, M., Canalizo, G., Rawlings, S., Sajina, A., Storrie-Lombardi, L., Armus, L., Marleau, F. R., & Muzzin, A. 2005, Mem. Soc. Astron. Italiana, 76, 154

Lacy, M., Petric, A. O., Sajina, A., Canalizo, G., Storrie-Lombardi, L. J., Armus, L., Fadda, D., & Marleau, F. R. 2007, AJ, 133, 186

Lawrence, A., et al. 2007, MNRAS, 379, 1599

Le Fèvre, O., et al. 2005, A&A, 439, 845

Lehmer, B. D., et al. 2005, ApJS, 161, 21

Lonsdale, C. J., et al. 2003, PASP, 115, 897

Maraston, C. 2005, MNRAS, 362, 799

Maraston, C., Daddi, E., Renzini, A., Cimatti, A., Dickinson, M., Papovich, C., Pasquali, A., & Pirzkal, N. 2006, ApJ, 652, 85

Middelberg, E., et al. 2008, AJ, 135, 1276

Miller, N. A., Fomalont, E. B., Kellermann, K. I., Mainieri, V., Norman, C., Padovani, P., Rosati, P., & Tozzi, P. 2008, ApJS, 179, 114

Muzzin, A., et al. 2009, ApJ, 698, 1934

———. 2011, preprint (arXiv:XXXXX)

Norris, R. P., et al. 2006, AJ, 132, 2409

———. 2011a, ApJ, 736, 55

———. 2011b, PASA, 28, 215

Oliver, S. J., et al. 2012, preprint (arXiv:XXXXX)

Owen, F. N., & Morrison, G. E. 2008, AJ, 136, 1889

Padmanabhan, N., White, M., Norberg, P., & Porciani, C. 2009, MNRAS, 397, 1862

Petric, A. 2010, in AIP Conf. Ser. 1240, Hunting for the Dark: The Hidden Side of Galaxy Formation, ed. V. P. Debattista, & C. C. Popescu (Melville: AIP), 76

Pierre, M., et al. 2007, MNRAS, 382, 279

Röttgering, H., et al. 2011, J. Astrophys. Astron., 32, 557

Rowan-Robinson, M., et al. 2008, MNRAS, 386, 697

Sanders, D. B., et al. 2007, ApJS, 172, 86

Schawinski, K., Thomas, D., Sarzi, M., Maraston, C., Kaviraj, S., Joo, S.-J., Yi, S. K., & Silk, J. 2007, MNRAS, 382, 1415

Silva, L., Granato, G. L., Bressan, A., & Danese, L. 1998, ApJ, 509, 103

Simpson, C., et al. 2006, MNRAS, 372, 741

Skrutskie, M. F., et al. 2006, AJ, 131, 1163

Smith, A. J., et al. 2012, MNRAS, 419, 377

Springel, V., et al. 2005, Nature, 435, 629

Surace, J. A., Shupe, D. L., Fang, F., Evans, T., Alexov, A., Frayer, D., Lonsdale, C. J., & SWIRE Team 2005, in BAAS, 37, 1246

Temporin, S., et al. 2008, A&A, 482, 81

Trichas, M., et al. 2010, MNRAS, 405, 2243

Ueda, Y., et al. 2008, ApJS, 179, 124

van Dokkum, P. G., et al. 2006, ApJ, 638, L 59

———. 2010, ApJ, 709, 1018

Weiß, A., et al. 2009, ApJ, 707, 1201

White, R. L., Becker, R. H., Helfand, D. J., & Gregg, M. D. 1997, ApJ, 475, 479

Wilkes, B. J., et al. 2009, ApJS, 185, 433

Willott, et al. 2010, http://adsabs.harvard.edu/abs/2010AJ....139..906W

Wilson, G., et al. 2009, ApJ, 698, 1943

Wright, E. L., et al. 2010, AJ, 140, 1868